# Magmatic Response to Subduction Initiation, Part II: Boninites and Related Rocks of the Izu-Bonin Arc From IOPD Expedition 352

John Shervais, Mark Reagan, Marguerite Godard, Julie Prytulak, Jeffrey Ryan, Julian Pearce, Renat Almeev, Hongyan Li, Emily Haugen, Timothy Chapman, et al.

# Magmatic Response to Subduction Initiation, Part II:

# Boninites and related rocks of the Izu-Bonin Arc from IOPD Expedition 352.

*John W. Shervais[1], Mark Reagan[2], Marguerite Godard[3], Julie Prytulak[4], Jeffrey G. Ryan[5], Julian Pearce[6], Renat R. Almeev[7], Hongyan Li[8], Emily Haugen[1§], Timothy Chapman[9,10], Walter Kurz[11], Wendy R. Nelson[12], Daniel Heaton[13], Maria Kirchenbaur[7,14], Kenji Shimizu[15], Tetsuya Sakuyama[16], Scott K. Vetter[17], Yibing Li[18], Scott Whattam[19]*

[1]*Department of Geology, Utah State University, Logan, UT, 84322-4505 USA john.shervais@usu.edu, ehaugen3@gmail.com*

[2]*Department of Earth and Environmental Science, University of Iowa, Iowa City, IA, USA mark-reagan@uiowa.edu*

[3]*Géosciences Montpellier, CNRS, Université de Montpellier, Montpellier, France Marguerite.Godard@umontpellier.fr*

[4]*Department of Earth Sciences, University of Durham, DH1 3LE, UK julie.prytulak@durham.ac.uk*

[5]*School of Geosciences, University of South Florida, 4202 East Fowler Ave., Tampa, FL 33604, USA ryan@mail.usf.edu*

[6]*School of Earth & Ocean Sciences, Cardiff University, Cardiff, UK PearceJA@cardiff.ac.uk*

[7]*Leibniz Universität Hannover, Institut für Mineralogie, Callinstrasse 3, D-30167, Hannover, Germany r.almeev@mineralogie.uni-hannover.de, m.kirchenbaur@mineralogie.uni-hannover.de*

[8]*State Key Laboratory of Isotope Geochemistry, Guangzhou Institute of Geochemistry, Chinese Academy of Sciences, Guangzhou 510640, PR China hongyanli@gig.ac.cn*

[9]*School of Geosciences, University of Sydney, Sydney, 2006 NSW, Australia t.chapman@sydney.edu.au*

[10]*Earth Sciences, School of Environmental and Rural Sciences, University of New England, Armidale, 2351 NSW, Australia* t.chapman@sydney.edu.au

[11]*Institute of Earth Sciences, NAWI Graz Geocenter, University of Graz, Austria walter.kurz@uni-graz.at*

[12]*Towson University, Dept. of Physics, Astronomy, and Geosciences, Towson University, Towson, MD 21252 USA wrnelson@towson.edu*

This article has been accepted for publication and undergone full peer review but has not been through the copyediting, typesetting, pagination and proofreading process, which may lead to differences between this version and the Version of Record. Please cite this article as doi: 10.1029/2020GC009093.

[13]*CEOAS, Oregon State University, Corvallis, OR, USA dheaton@ceoas.oregonstate.edu*

[14]*Institut für Mineralogie, Universität zu Köln, Zülpicher Str. 49b,50674 Köln, Germany*

[15]*Kochi Institute for Core Sample Research, Japan Agency for Marine-Earth Science and Technology, Kochi, 783-8502 Japan shimmy@jamstec.go.jp*

[16]*Department of Science, Osaka University, Sumiyoshi-ku Osaka 558-8585 Japan sakuyama@sci.osaka-cu.ac.jp*

[17]*Department of Geology, Centenary College, Shreveport, LA. 71104 USA svetter@centenary.edu*

[18]*Institute of Geology, Chinese Academy of Geological Science, Beijing 100037, P.R. China yibingli@cags.ac.cn*

[19]*Department of Geosciences, King Fahd University of Petroleum and Minerals, Dhahran 31261, Saudi Arabia sawhatta@gmail.com*

*§Current Address: Department of Geology, California State University, Sacramento, Sacramento, CA, USA*

Key Points: (1) Boninite forms by fluid-flux melting of previously depleted mantle in response to subduction initiation, where early boninites, which form at an axial spreading center, are low in silica and have $La_{ch}/Sm_{ch}$ <1.0. (2) later boninites form off-axis; they are higher in silica and have $La_{ch}/Sm_{ch}$ >1.0. (3) the early low-Si boninite source is enriched by partial melts of altered ocean crust; the later high-Si boninite source is enriched by partial melts of sediment as well as altered ocean crust.

Index Terms: **1031, 1065, 3640, 3036**

Keywords: **Boninite, Izu-Bonin-Mariana Forearc, subduction initiation, ophiolites, IODP Expedition 352, Sites U1439, U1442, JOIDES Resolution**

## ABSTRACT

International Ocean Discovery Program Expedition 352 to the Izu-Bonin forearc cored over 800 m of basement comprising boninite and boninite-series lavas. This is the most extensive, well-constrained suite of boninite series lavas ever obtained from *in situ* oceanic crust. The boninites are characterized as *High-Silica Boninite* (HSB), *Low-Silica Boninite* (LSB) or *Basaltic Boninite* (BB) based on their $SiO_2$-MgO-$TiO_2$ relations. The principal fractionation products of all three series are *High-Mg Andesites* (HMA). Lavas recovered >250 meters below the seafloor (mbsf) erupted at a forearc spreading axis and are dominated by LSB and HMA. Lavas recovered from <250 mbsf erupted off-axis and are dominated by HSB. The axial and off-axis lavas are characterized by distinct chemostratigraphic trends in their major, trace, and isotopic compositions. The off-axis lavas are chemically similar to boninite from the type locality at Chichijima, with concave-upward REE patterns. In contrast, the more abundant axial lavas have distinctly LREE-depleted patterns and represent a new, previously unsampled precursor to the Chichijima-type boninite lavas. Petrogenetic modeling suggests that the axial lavas formed by fluxing of refractory mantle (likely the residue from fore-arc basalt extraction), with amphibolite-facies melt derived from subducting altered oceanic crust. The upper, off-axis lavas require an additional component of sediment-derived melt in addition. Both models are consistent with previously published isotopic data.



## PLAIN LANGUAGE SUMMARY

Lavas erupted in the forearc of the Izu-Bonin-Mariana arc, and sampled by IODP Expedition 352, include unusual highly primitive compositions characterized by both high MgO and high $SiO_2$ concentrations. These are termed ‘boninite’, after their type locality in the nearby Bonin Islands. We divide these lavas into three suites distinguished by high-silica, low-silica and very low (basaltic) silica contents. The basaltic boninite and low-silica boninite make up the deepest part of the volcanic section (>250 meters below sea floor) and are interpreted to have formed at an axial spreading center. Lavas less than 250 meters below sea floor erupted later, in an off-axis setting, and consist of high-silica boninite. Both groups formed by melting of mantle depleted by a prior episode of melting, in response to the addition of water-rich melt derived from subducting oceanic crust. Formation of the off-axis high-silica boninite required the further input of melt derived from subducted sediment.

## Introduction

Boninites are highly refractory volcanic rocks commonly associated with nascent subduction zones. The type locality for boninite is Chichijima (Bonin Island) in the Izu-Bonin-Mariana (IBM) forearc in the western Pacific Ocean (e.g., *Peterson, 1891; Kuroda and Shiraki, 1975; Umino, 1986; Dobson et al, 2006; Ishizuka et al, 2020*). Boninites exhibit distinct chemical features that may be linked to their tectonic setting(s). For instance, they are characterized by high MgO (>8 wt%) and $SiO_2$ (52-63 wt%), together with low $TiO_2$ (<0.5 wt%), which sets them apart from typical mid-ocean-ridge or intraplate basalt (*e.g., Crawford et al, 1989; Pearce and Robinson, 2010; Pearce and Reagan, 2019*). The canonical interpretation of the chemistry of boninites is that they result from low pressure melting of previously depleted mantle sources, and that these sources must be fluxed with fluid to permit such melting (*e.g., Cameron et al., 1979, 1985; Meijer, 1980; Hickey and Frey, 1982; Crawford et al, 1989*), an interpretation supported by melting experiments (*e.g., Van der Laan et al., 1989; Umino and Kushiro, 1989; Falloon and Danyushevsky, 2000; Mitchell and Grove, 2015*) and geochemical modelling (e.g., König et al. 2010). Lavas with boninite compositions may erupt in alternative tectonic settings such as those associated with intra-oceanic mantle plumes or near-trench volcanism in established oceanic arc-basin systems (*e.g., Sobolev and Danyushevsky, 1994, Deschamps and Lallemand, 2003; Falloon et al, 2008; Ribeiro et al., 2015*). However, most boninitic lavas of <2 Ga age do link strongly with other indicators of subduction initiation (e.g., *Meijer, 1980; Hickey and Frey, 1982; Bloomer and Hawkins, 1987; Walker and Cameron, 1983; Crawford et al, 1989).* As a consequence, boninites provide a means of fingerprinting the onset of subduction in the rock record and through a significant period of geologic time (*Pearce and Reagan 2019*).

A key challenge in using any lithology as a fingerprint of tectonic setting is nomenclature and classification. Typically, boninites have been characterized by their MgO-$SiO_2$-$TiO_2$ systematics. However, many boninites in the rock record have undergone metamorphism, and many are erupted in the submarine environment, with both processes offering the ability to alter $SiO_2$ and MgO contents. *Pearce and Reagan (2019)* have recently re-visited the original IUGS classification scheme for boninites, and have provided an updated assessment, taking into account worldwide boninite occurrences, careful screening for alteration, and the unique petrology of these rock types. *Pearce and Reagan (2019)* will therefore be the basis for classification used throughout this study.

Expedition 352 of the International Ocean Discovery Program (IODP; *Reagan et al, 2015a; 2017, 2019*) was designed to investigate the magmatic response to subduction initiation in the IBM forearc near Chichijima (Bonin Island). The lack of significant collisional deformation makes the IBM system ideal for understanding the magmatic response to subduction initiation. Boninite in

the IBM arc system predates the main volcanic arc. As a result, early workers concluded that the first magmas erupted after subduction initiation were boninitic (*Cameron 1985; Crawford et al, 1989; Pearce et al, 1992*). However, *Reagan et al (2010)* discovered that IBM boninites were preceded by MORB-like basalts which they termed *forearc basalts* (FAB), also referred to as *proto-arc basalts* by *Umino et al. (2015*). They demonstrated that FAB formed largely or entirely by decompression melting with little slab flux. In addition, *Reagan et al. (2019)* present new Ar-Ar ages which show that FAB are <600 ka older than the boninites.

IODP Expedition 352 drilled an *in situ* magmatic record of the initiation of subduction of the Pacific Plate beneath the Philippine Sea Plate. Drilling allowed recovery of samples that have largely escaped the effects of seawater alteration, and, in many cases, still retain fresh glass (*Reagan et al., 2015a-e*). The rocks from Expedition 352 have also been studied for their radiogenic isotopic composition (*Li et al., 2019*), their ages have been determined with high precision whole-rock Ar-Ar geochronology (*Reagan et al., 2019*) and all holes were surveyed in real time onboard the JOIDES Resolution by portable XRF, creating a high resolution chemostratigraphy (*Ryan et al., 2017*). This plethora of chemical data has allowed truly representative sampling of all major units recovered in the core, and offer unprecedented context to examine the genesis of the boninites.

*Shervais et al. (2019)* presented a detailed assessment of FAB sampled by Expedition 352 at Sites U1440 and U1441 (*Reagan et al, 2015b, 2015c*), and established the likely means of generation of FAB underlying the Bonin forearc. They demonstrated that FAB were the product of extensive melting of old, partially depleted oceanic mantle, with no significant slab flux. This work has also provided a well-constrained baseline from which to examine the subsequent genesis of the boninitic lavas spatially and temporally associated with FAB. We present new data on the petrogenesis of boninite and related rocks at Sites U1439 and U1442, the drill cores from which contain the most continuous and chemically pristine series of *in situ* boninitic rocks so far recovered (*Reagan et al, 2015d, 2015e*). Specifically, the recovered cores allow us to (1) determine the extent of chemical and petrologic variability for Expedition 352 boninite, and so provide insight into the dominant processes that create such variability, and (2) create and test detailed, self-consistent geochemical models for the generation of boninite to determine whether their petrogenesis is linked to the residual FAB source.

## GEOLOGIC SETTING

The Izu-Bonin-Mariana (IBM) system is a convergent plate boundary that currently stretches over 3,000 km from the Izu Peninsula (Japan) in the north to Palau in the south (Figure 1) (*Stern et al. 2003; Ishizuka et al, 2006; Wu et al 2016*), between an upper Philippine Sea plate and a

subducting Pacific plate. Subduction began in the early Eocene, circa 52.5 Ma, shortly after the collision of India with mainland Asia and shortly before the Hawaii-Emperor chain inflection (*Meade, 2007; Najman et al., 2010; Ishizuka et al., 2011a, 2018; Reagan et al., 2013; 2019*; *Wu et al 2016*). The Parece Vela and Shikoku backarc basins began forming circa 25 Ma (*Ishizuka et al., 2011b*), leaving the Kyushu-Palau ridge remnant arc to the west (*Mrozowski and Hayes, 1979; Okino et al., 1998*). The West Philippine Basin is a backarc basin that opened between about 52 Ma and 30 Ma (*Savov et al., 2006a; Deschamps and Lallemand, 2002; Ishizuka et al., 2013*).

The IBM forearc includes prominent ridges capped by islands (e.g. the Bonin Islands at 26-28ºN latitude, Saipan at c. 15ºN, and Guam at 13.5ºN), with fault-bounded and asymmetric extension-related basins (i.e., half-grabens) containing pelagic and volcaniclastic sediments stepping down to the trench (*Chapp et al., 2008; Christeson et al., 2016; Robertson et al., 2018, Kurz et al., 2019*). Sedimentation on the trench slope was syn-tectonic, with the lowermost, Oligocene to Early Miocene sedimentary units dipping relative to the overlying younger sediments (*Kutterolf et al., 2018; Robertson et al., 2018*).

The IBM forearc where sampled along its entire length has a geological succession similar to that of many ophiolites, with boninites, FAB, dolerites, gabbroic rocks and depleted peridotites cropping out progressively down the trench slope (e.g. *Meijer et al., 1981; Bloomer, 1983; Stern and Bloomer, 1992; Parkinson and Pearce, 1998; DeBari et al., 1999; Morishita et al., 2011; Reagan et al., 2013*). *Ishizuka et al. (2011a) and Reagan et al. (2019)* document the age of this crust and show that it is essentially synchronous over 1700 km of strike. This remarkably extensive and near-simultaneous burst of new crust formation above a nascent subduction zone provides our best in-situ analogue for subduction initiation yet studied.

IODP Expedition 352 drilled four sites in the southern Izu-Bonin arc near the Ogasawara (Bonin) island group. The two relatively trench-distal sites (U1439 and U1442) recovered boninite, and the two relatively trench-proximal sites (U1440, U1441) recovered forearc basalts (Figure 1). Site selection was based on the results of dredging and submersible dives, which showed that boninite occupies the shallow inner wall of the trench, topographically and (apparently) stratigraphically above forearc basalt and gabbro (*Ishizuka et al., 2011a*). The two boninite suite holes are (Figure 2):

(1) U1439C (28°24.4491'N, 142°36.5368'E); 3129.2 m water depth; 362.3 m cored and 107.8 m recovered; 544.3 mbsf (meters below sea floor) total penetration: 182.0 m of sediment, 362.3 m of basement.

(2) U1442A (28°24.5784'N, 142°37.3368'E); 3162.0 m water depth; 529.8 m cored with 100.7 m recovered; 539 mbsf total penetration: 83.12 m of sediment, 446.68 m of basement.

In addition, a third hole consisting largely of sediment drilled adjacent to U1439C recovered boninite that appears to be contiguous with Unit 1 of U1439C:

(3) U1439A (28°24.4487' N, 142°36.5120' E); 3128.1 m water depth; 199.4 m cored with 170.7 m recovered, mostly sediment but with some boninite at the base (*Kutterolf et al, 2018; Robertson et al., 2018*).

Although these sites were targeted to drill through boninite into FAB, they encountered only boninite suite lavas and intrusive rocks (*Reagan et al., 2017*).

**METHODS**

Sixty-eight samples were chosen from Holes U1439A, U1439C, and U1442A. Approximately 2-3 g of each sample was reduced to chips and sonicated in deionized water repeatedly until the water remained clear, then dried and powdered in a tungsten carbide shatterbox. Approximately 1.4 g of powder was mixed with 9.8 g of lithium tetraborate flux (1:7 ratio) and fused to form a glass bead for X-ray fluorescence analysis. The glass beads were analyzed for major elements and selected trace elements with a *Panalytical® 2400* sequential XRF spectrometer at Utah State University, calibrated using a suite of 20 international rock standards (*U.S. Geological Survey, Siberian Institute of Geochemistry, Japan Geological Survey*). Count rates were corrected for absorption and secondary fluorescence using fundamental parameters in the Panalytical® SuperQ® software. A split of ~50 mg was dissolved using hydrofluoric and nitric acid and analyzed with a Perkin-Elmer Nexion 2000 ICP-MS for the rare earth elements (REE) and 10 other trace elements. $CO_2$ analyses were carried out with a *Costech Elemental Analyzer* at Utah State University. We assume that all $CO_2$ is present as calcium carbonate, and does not include significant high-Mg calcite or dolomite. On this basis, we correct the analyzed CaO content to remove its effect using the correction: $CaO^* = CaO - (CO_2 * 56/44)$, where CaO* represents CaO in the silicate portion of the sample. Sample compositions are then normalized (for all elements) to 100%. This correction is most important for samples with high carbonate content, *e.g.*, filling vesicles, and may affect how they are classified. There is no correlation between $CO_2$ and Sr content, so most Sr is assumed to reside in silicates. Representative samples leached with cold acetic acid document that most trace elements, in particular, the REE, the high field strength elements, Pb, U and Th, are not affected by carbonate deposition (all below detection in the leachates), and that Sr enrichment from carbonate in the whole rocks analyses is typically less than 10-20 µg/g (less than the symbol size on plots). Whole rock major and trace element chemistry for

these samples is presented in Supplemental Data Table DS01 and archived in the Pangaea data archive (*Shervais et al., 2020).* Results of the acetic acid leaching experiments are presented in Supplemental Data Set DS06.

In addition to the personal samples described above, oxidized powders from 70 shipboard samples that were analyzed by ICP-AES during the expedition were analyzed here by XRF only, using the same procedures. Carbonate correction was applied using the shipboard $CO_2$ analyses (*Reagan et al. 2015f*). Sample preparation is described in *Reagan et al. (2015f)* and the data are presented in Supplemental Data Table DS02 and the Pangaea data archive (*Shervais et al, 2020*).

Expedition 352 scientists used a hand-held portable XRF (pXRF) shipboard to monitor chemical variations in the basalts as part of the core logging process (*Ryan et al., 2017*). Data from the pXRF were regressed against shore-based XRF data to determine how well they correlate, and the pXRF concentrations adjusted if needed to remove analytical bias (e.g., $Cr = Cr_{pXRF}*1.28+9.8$; $Zr = Zr_{pXRF}*1.38-5.8$). No adjustment was made for regressions within 5% of shore-based XRF values ($K_2O$, $TiO_2$, Sr, V). These data are used to supplement shore-based data for the chemostratigraphy, but not for geochemical modeling. During shipboard sampling, pXRF data were used to help select both the POOL and personal samples, and proved critical in defining chemostratigraphic units and unit boundaries (*Reagan et al., 2015a*).

The following terms used to classify boninite (see below) are defined as follows: $Si8= SiO_2+(MgO-8)/3.82$, $Ti8= 42*TiO_2/(50-MgO)$, and $Sr8= 42*Sr/(50-MgO)$. These algorithms project lava compositions to MgO = 8% using olivine control lines from olivine (Fo90) + orthopyroxene for Si8 and olivine (for Ti8 and Sr8) (*e.g., Pearce and Reagan, 2019*).

## RESULTS

### Classification and Nomenclature

The classification of boninites and other high-MgO volcanic rocks was formalized by the IUGS (*Le Bas, 2000*), who defined boninites as having $SiO_2$>52 wt%, $TiO_2$<0.5 wt%, and MgO>8 wt%. *Pearce and Robinson (2010)* revisited the classification scheme, considering the petrology of the rock type, specifically that they would have olivine ± opx as the near liquidus assemblage, and thus a rectangular box-like classification was inappropriate. Further, early work recognized the existence of evolved rocks (high-Mg andesites) related to boninites by fractionation (*e.g., Meijer 1980*) that are distinct from normal volcanics of the basalt-andesite-dacite-rhyolite series. Recently, *Pearce and Reagan (2019)* revised their classification scheme, taking advantage of the expanded databases for MORB and motivated in part by the wide variety of boninitic rocks recovered by Expedition 352. In this paper, we follow the conventions proposed by *Pearce and*

*Robinson (2010)* and *Pearce and Reagan* (2019), in which boninite field boundaries are olivine control lines (or olivine ± orthopyroxene control lines for silica), and high-Mg andesite/dacite form a field at higher MgO than normal arc volcanics (Figure 3).

Figure 3 summarizes the distinct geochemical lava types found at Sites U1439 and U1442. The dominant rock type at Sites U1439 and U1442 is boninite, with high MgO (>8 wt%), high $SiO_2$ (52-63 wt%) and very low $TiO_2$ (<0.5%). The second most abundant rock type is high-Mg andesite (HMA), which has similarly high silica and low $TiO_2$ contents, with MgO higher than normal calc-alkaline andesite and dacite but less than 8.0 wt% (Figure 3A). Calc-alkaline andesite of the BADR series is a rare rock type at Sites U1439 and U1442.

Boninites are subdivided into *High-Silica Boninite* (HSB) and *Low-Silica Boninite* (LSB) using the approach of *Pearce and Reagan* (2019). We also recognize a *Basaltic Boninite* (BB) subdivision of the LSB field, following Expedition 352 Shipboard Party classification (*Reagan et al., 2017*). Basaltic boninites are those that fall into the low-silica corner of the IUGS boninite field or plot outside the IUGS boninite field at less than 52% $SiO_2$ on olivine control lines that would move them into the IUGS boninite field with fractionation (Figure 3; *Reagan et al 2017*); these are equivalent to the *ultra-low silica boninites* of *Umino et al (2015).* Basaltic boninite and some LSB correspond to high-Ca boninite of Crawford (1980), whereas most LSB and all HSB correspond to low-Ca boninite.

Field boundaries at 8% MgO are taken from *Pearce and Reagan (2019),* at 52%, 57% and 63% $SiO_2$ (Figure 3A). Field boundaries for BB and LSB are projected to an Fo92 olivine composition (51% MgO, 41% $SiO_2$). The lower BB boundary line runs from 52% $SiO_2$ at 8% MgO to 47.7% $SiO_2$ at 25% MgO, while the BB-LSB boundary runs from 54% $SiO_2$ at 8% MgO to 49.9% $SiO_2$ at 25% MgO. The upper boundary of the HSB field follows the convention of *Pearce and Reagan (2019)* as an Opx-control line from 63% $SiO_2$ at 8% MgO to 57% $SiO_2$ at 32% MgO (enstatite). The LSB-HSB boundary is an olivine-Opx control line from 57% $SiO_2$ at 8% MgO to 53.5% $SiO_2$ at 20% MgO; this is equivalent to a fractionating assemblage of ~2:1 olivine:enstatite (Figure 3A). Boninite is also characterized by $TiO_2$ <0.5% at MgO>8% (Figure 3B). In Figure 3C, BB, LSB, and HSB have distinct trends in $SiO_2$ vs $TiO_2$ space.

*Pearce and Reagan (2019*) used a plot of Si8 *versus* Ti8 ($SiO_2$ and $TiO_2$ projected to 8% MgO), to combine the salient features of both the $SiO_2$-MgO and MgO-$TiO_2$ plots. The Si8-Ti8 plot clearly place almost all Site U1439 and Site U1442 lavas in the *boninite suite* field, with the exception of some highly altered basaltic boninite samples, which plot as Low-Ti basalts (Figure 4) due to loss of Si *(Pearce and Reagan, 2019)*. In contrast, FAB-suite lavas from Sites U1440

and U1441 plot largely in the *basalt-andesite-dacite-rhyolite* (BADR) field, as do nearly all MORB (Figure 4). A plot of Ti8 vs Sr8 (Sr projected to 8% MgO) shows the mantle depletion trend of oceanic basalts (Figure 4B). Boninite series rocks of Expedition 352 are more depleted in $TiO_2$ (very low Ti8), but enriched in Sr8, which is inferred to represent the influence of slab-derived melts on the depleted mantle wedge.

**Volcanic Stratigraphy and Structure**

Stratigraphic columns for Holes U1439C and U1442A are presented in Figure 2, which includes unit descriptions, core numbers, and core recovery (*Reagan et al. 2015d, 2015e*). Also shown are depths with slip surfaces, brecciation, or other evidence for faults.

***U1439A:*** Hole U1439A produced 10 cores and 13 extended core barrel (XCB). Three of the XCB penetrated basement. The basement contains a single igneous unit: a hyaloclastite breccia with centimeter-scale pillow fragments and glass in an altered glass matrix. The uppermost breccia is separated from the overlying calcareous ooze by a Mn-rich crust about 1 cm thick. The overlying sedimentary section is discussed by *Robertson et al. (2018)* and *Kutterolf et al. (2018),* who present a stratigraphic column for this hole.

***U1439C:*** Hole U1439C encountered basement at 182.0 mbsf and penetrated 357 m of basement, to a depth of 539 mbsf. This hole comprises 10 igneous units, nine of which are volcanic and the other (Unit 10) is interpreted as a hypabyssal intrusive complex (Figure 2A). The most common flow type in the volcanic units is pillow lava (Units 3a, 4, 5, 6, 8, and 9). Pillow structures are inferred from curved chilled margins oblique to the vertical axis of the core, radial fractures that emanate from a massive core, or glassy outer surfaces. Two units (6, 9a) contain what appear to be “mega-pillows” with diameters of 1-2 m that are intercalated with smaller pillows, and may represent feeders to smaller pillow lobes. In Unit 5, some of the larger pillows appear to have accumulated olivine and pyroxene in their lower portions, leaving the upper portions aphyric or crystal-poor. Massive sheet flows are much less common (Units 2a, 7), but may also be intercalated within pillow flows (Unit 9a). Pumice-rich hyaloclastites, which may represent submarine pyroclastic flows, are confined to HSB lavas in the upper part of the hole (Units 2b, 3b). More common are inter-pillow breccias and hyaloclastites (Units 3a, 5, 6, 8). The deepest unit in the Hole (Unit 10) is dominated by dolerites.

The most striking features in this core are the magma-mingling structures seen in Unit 8 (U1439-28R through U1439-35R; Figure 5A-C). Pale-gray, evolved LSB-HMA with chilled margins mingle with darker gray, more primitive high-Cr lavas. These two components of the core were distinguished during logging with the pXRF instrument (*Ryan et al., 2017*). This mingling is

also clearly evident in the chemostratigraphy, as discussed below, and in Hole U1442A (Figure 5D-E).

***U1442A:*** The stratigraphy of Hole U1442A is relatively simple (Figure 2B), consisting of four units. Despite its proximity to U1439C, however, it differs significantly from that hole in a number of ways. The dominant flow type in U1442A is hyaloclastite breccia/lapillistone, consisting of moderately to highly vesicular pumice lapilli in a matrix of finer-grained ash and its alteration products (Figure 5F). Unit 1 comprises five subunits. Of these, Subunits 1a, 1c, and 1e are all HSB hyaloclastite breccia or lapillistone, 30-55 m thick, which may represent submarine pyroclastic flows. Pumice lapilli are up to 6 mm in diameter and contain up to 25% vesicles. Subunit 1e contains some intermingled HMA, similar to those in Unit 2. Subunits 1b and 1d are massive or pillowed HSB lavas forming intercalations 13-28 m thick (Figure 2B). Unit 2 consists of two subunits: Subunit 2a is a hyaloclastite comprising BB and LSB pumice intermingled with HMA lavas, which may be distinguished by their high magnetic susceptibilities; Subunit 2b comprises massive sheet flows of HMA (Figure 2B). Unit 3 is another hyaloclastite, 68 m thick, of HMA composition. Interspersed with the hyaloclastite are flows of lighter colored lava that appear to have invaded the hyaloclastites before lithification, much like a peperite. The lighter-colored lava is chilled against the glassy breccia with irregular lobate contacts. In some places, magma mingling created diffuse cuspate contacts between dark- and light-colored magmas, similar to those in Hole U1439C Unit 8 (Figure 5DE). Glassy margins show that one magma has quenched against the other more crystalline magma, but the cuspate margins are consistent with a magma-magma intrusive contact.

**Petrography and Microstructure**

Phenocryst abundances are shown in Figure 6 as a function of depth (A: U1439C, B: U1442A). Representative photomicrographs are presented in Figure 7, and mineral compositions are reported by *Whattam et al. (2020).* Some samples have phenocryst abundances of 20-40% by volume, which indicates significant crystal accumulation, although most are typically ~8 to 15% (Figure 6). This is supported by major element compositions, as discussed below. A number of samples are characterized by secondary calcite deposition, particularly filling vesicles in pumice fragments and lavas, and along fractures. These samples were corrected to calcite-free compositions as described in the Methods section.

***High-Silica Boninites (HSB):*** HSB are characterized by phenocrysts of enstatite (0.7-0.9 mm; up to 40%; average 6.7%) and olivine (0.5-0.9 mm; up to 10% by volume; average 3.6%), with enstatite typically more abundant than olivine (Figure 7A, B). Augite is rare (≤1% in one sample, 0.3 mm), and plagioclase is not found as either a phenocryst or a groundmass phase. Textures are

commonly vitrophyric with pale tan glass containing acicular pyroxene needles (~26% enstatite, 17% augite; Figure 7C-F). Pyroclastic textures dominate U1442A Unit 1, with glassy-rich pumice lapilli in a matrix of glass shards and crystals. Magma mingling textures are evident in U1442A Unit 1, where cuspate contacts and glassy chilled margins document magma-magma mingling (Figure 7GH).

***Low-silica Boninites (LSB):*** LSB are characterized by abundant phenocrysts of olivine (0.7-0.9 mm; up to 30%; average 11%) with less common low-Ca pyroxene (0.7 mm; 2.2%) and augite (0.4-0.6 mm; 2.6%) on average, and trace Cr-spinel (≤1%) commonly forming inclusions in olivine (Figure 7I-J). Plagioclase phenocrysts are rare and small (≤0.5 mm). Augite forms acicular needles or overgrowths on low-Ca pyroxene. The groundmass is typically glassy (~70% glass) or microcrystalline with 20-40% augite, 10-20% low-Ca pyroxene, and 40-50% plagioclase. LSB in Unit 10 have fine-grained doleritic textures, indicative of a shallow intrusive origin (Figure 7K-L).

***Basaltic Boninites (BB):*** BB are characterized by euhedral/prismatic phenocrysts of olivine (up to 20%; average 6%), with less common orthopyroxene (~3.2%) and relatively common augite (2-5%) either as discrete phenocrysts or as overgrowths on low-Ca pyroxene (Figure 7M-N). Olivine may be large (up to 7 mm; average 1.8 mm), while pyroxene is generally smaller (average 1.4 mm). Cr-Spinel is common (1-4%) as small (<1 mm) grains. The groundmass is typically glassy (30-50% glass), or microcrystalline with 20-40% augite, 10-20% low-Ca pyroxene, and 40-50% plagioclase. Unit 7 altered basaltic boninite is moderately olivine-augite phyric with ~5% olivine and ~7% augite phenocrysts (all ~0.6 mm in size) in a microcrystalline intersertal matrix of augite and plagioclase.

***High-Mg Andesites:*** HMA are sparsely porphyritic with augite ± olivine ± plagioclase phenocrysts (all ~0.5-0.8 mm) in a fine-grained to microcrystalline, intersertal to intergranular plagioclase-rich matrix (Figure 7OP). Trachytic textures are common.

***Andesites (U1439C, Unit 4):*** Augite (0.6 mm; ~2%) and plagioclase (0.4 mm; ~1%) phenocrysts in an intersertal, plagioclase-rich groundmass.

**Geochemistry**

*Major Elements:* The major element geochemistry of lavas from U1439 and U1442 has already been largely discussed in the section on classification and nomenclature. $TiO_2$ and $SiO_2$ both increase with decreasing MgO. In contrast to fore-arc basalts (FAB), mid-ocean ridge basalts (MORB), and island arc tholeiites, boninite-suite lavas follow iron-depletion trends with

decreasing MgO, similar to calc-alkaline suite lavas (Figure 8A). Alkalis are high, with $Na_2O$ <3.0% and $K_2O$ <1.0% typically. CaO* (CaO in silicate phases) is generally lowest in the HSB, and increases progressively in LSB and BB as silica decreases. Samples with >13% MgO are too magnesian to be in equilibrium with even refractory mantle ($Fo_{92}$) and likely have accumulated olivine and/or orthopyroxene; this is supported by high phenocryst loads discussed above.

Lavas with low silica and MgO <8.0 wt%, but with characteristics of boninite (*e.g.*, $TiO_2$ <0.5 wt%, Cr = 900-1100 ppm), are common in Units 9-10 of U1439C. We infer from the high Cr concentrations that these samples are likely highly altered boninite that have lost both MgO and $SiO_2$ during hydrothermal alteration.

*Trace elements:* The high field strength incompatible elements such as Zr and Nb, the rare earth elements (REE), and Y define tight linear trends on MgO-variation diagrams. These elements are consistently lower in concentration than in MORB or FAB, with little enrichment over the range of MgO (Figure 8B, C, D, E). In contrast, Sr concentrations in the boninite suite overlap MORB at low MgO, whereas FAB have Sr at the lowest end of the MORB field (Figure 8F). Elements sensitive to low-temperature alteration *(e.g.,* K, Rb) display a wide range in concentrations that are independent of MgO concentration. Elements less mobile at low-temperatures (Sr, Ba, Pb) have more consistent concentrations between samples, indicating that these elements have not been greatly affected by low-temperature alteration in most samples chosen for analysis. All of these elements are enriched in boninite relative to FAB. Compatible elements such as Cr, Ni and Co all decrease as MgO decreases.

Ti/V ratios are extremely low, with HSB Ti/V $\leq$ 10, and LSB-BB-HMA Ti/V = 10-14 (Figure 9A, B). In contrast, FAB from Sites U1440 and U1441 have Ti/V = 10-20, but at much higher concentrations (>250 µg/g V), whereas contemporaneous rear-arc basalts sampled by Expedition 351 (U1438) have ratios ~15-21 with V concentrations ~200-300 µg/g (Figure 9A). The sub-chondritic Ti/V ratios of boninite were highlighted by *Shervais (1982),* who attributed this feature to re-melting of previously depleted sources at high $fO_2$. Zr/Sm ratios of boninite suite rocks are high (25-70) at very low Sm concentrations (<1.5 µg/g; Figure 9B). In general, off-axis HSB have the highest Zr/Sm (36-74; average ~46) while LSB-BB have the lowest ratios (24-50; average ~36). FAB have Sm concentrations of 1-3 µg/g but with significantly lower Zr/Sm ratios (~12-22), whereas MORB have intermediate Zr/Sm ratios (~20-35) at high Sm concentrations (>1.5 µg/g).

Rare-earth elements (REE) define chemical groups correlated with depth, as seen in chondrite-normalized REE plots (Figure 10: C1 chondrite values of *Sun and McDonough, 1989*). A few

samples have significant negative Ce anomalies, indicating REE mobility resulting from alteration (*Patino et al., 2003*), but most have relatively smooth chondrite-normalized patterns indicating little or no impact from low-temperature alteration. At Site U1439, samples ≤250 mbsf (Units 1-4) are largely HSB but include some LSB; Unit 4 is andesite. These samples have spoon-shaped chondrite-normalized patterns, with a small range in HREE (3.5-6x C1), a larger range in LREE (3-9x C1), normalized La/Sm ≥1.1, and a minimum centered near Dy (Figure 10A). Samples >250 mbsf (Units 5-10) are largely LSB with less common BB and HMA. These samples have relatively flat to slightly left-sloping MREE-HREE concentrations (~3-7x chondrite) and distinct LREE-depletion ($La/Sm_{ch}$ ≤0.95). The LREE-depletion becomes more pronounced at shallower depths (Figure 10B, C, D).

At Site U1442, samples ≤250 mbsf are HSB with minor LSB. As for Site U1439, most of these samples have spoon-shaped chondrite-normalized patterns, with a small range in HREE (3.5-6x C1), a larger range in LREE (2.5-8x C1), normalized La/Sm ≥1.0, and a minimum centered near Ho (Figure 10E). Samples in the interval ~180-250 mbsf (Subunit 1e) have a pronounced dip in LREE concentration such that C1-normalized La/Sm has values of ~0.95-1.3; this unit contains some intermingled HMA lavas. U1442A samples >250 mbsf are largely HMA and LSB with minor HMD and HSB (transitional to LSB). These samples have relatively flat MREE-HREE patterns, with slight LREE-depletion (normalized La/Sm <0.94). In general, HMA and HMD have higher REE concentrations than LSB (Figure 10F-G).

MORB-normalized multi-element (spider) diagrams generally display a slight negative slope from Nd to Y, with an upturn to flat or slightly positive slopes from Y to Lu. In general, more incompatible elements are progressively enriched compared to less incompatible elements (Figure 11). Fluid-mobile elements susceptible to low-temperature mobility (e.g., K, Rb) have variable and inconsistent concentrations, suggesting that these concentrations have been affected by alteration. Titanium displays small and inconsistent negative anomalies. In contrast, Nb is characteristically depleted relative to adjacent elements (e.g., Th, La), giving negative anomalies, though not as pronounced as in most normal arc volcanics. Th/La is generally >1x MORB.

MORB-normalized Zr-Hf relative to their adjacent REE (Nd, Sm) generally correlate with depth in the core: samples from >250 mbsf have normalized concentrations of these elements with small positive anomalies relative to adjacent REE, whereas samples ≤250 mbsf have distinct positive anomalies (Figure 11; see also Figure 9B, where MORB Zr/Sm ~28).

*Chemostratigraphy:* Expedition 352 scientists created a chemostratigraphic framework for Holes U1439C and U1442A using the shipboard pXRF (*Ryan et al, 2017*). This framework was

used to guide sampling for shore-based work, allowing us to confirm the overall validity of the framework and to refine it. This approach was especially useful for distinguishing between the diverse chemical groups present, so allowing us to develop a stratigraphic framework despite their petrographic similarity. Chemostratigraphic trends of $TiO_2$, Ti/V, Ti/Zr, Zr/Sm and La/Sm for Holes U1439C and U1442A are shown in Figures 12 and 13, respectively. There are distinct breaks at ~250 mbsf in most of these profiles, with lavas <250 mbsf characterized by lower $TiO_2$, Ti/V and Ti/Zr, and higher Zr/Sm and La/Sm than those >250 mbsf (Figures 12, 13). For both holes, lavas <250 mbsf are dominated by HSB and HMA related to HSB, whereas lavas >250 mbsf are dominated by LSB, BB, and HMA related to LSB.

**Magma Mixing and Magma Mingling**

Magma mixing and magma mingling appear to be common processes in the Expedition 352 boninite suite lavas, as it is, for example, in the boninite type locality of Chichijima (*Umino, 1986*). Magma mingling is clearly documented in the core by more primitive lavas intruding and physically mingling with more evolved lavas or hyaloclastites (e.g., Figure 5). Detailed chemostratigraphic plots reveal other stratigraphic horizons dominated by magma mixing, where more- and less-evolved magmas have mixed to form a range of intermediate compositions. These horizons are especially evident in plots supplemented with pXRF data (*e.g.,* $TiO_2$), which may document multiple intermediate compositions not captured in the shore-based data. Cryptic mixing may also have occurred in places where mixing was sufficient to form a single intermediate composition; in this case, evidence for mixing is only preserved as zoning profiles and overgrowths in phenocrysts.

**PETROGENETIC MODELING**

Petrogenetic models can be used to address several aspects of boninite origin: (1) fractionation of primary magmas to form the observed range of boninite and HMA compositions; (2) partial melting to form the primary magmas, (3) contribution of melt components not derived from mantle melting, i.e., partial melts of subducting oceanic crust and sediments; and (4) calculation of equilibrium P-T conditions during partial melting. Major goals of our modeling are to refine the conceptual model of boninite petrogenesis, as constrained by the radiogenic isotopic data of *Li et al. (2019),* to assess the distinction between LSB and HSB, which we infer below to represent volcanism at an axial spreading center and off-axis, respectively, and to assess linkages between boninite petrogenesis and subduction initiation. Potential parental magma compositions have MgO ~13-14 wt%, based on equilibrium with residual mantle of $Fo_{92}$ composition. $Fo_{92}$ residual mantle was chosen based on the highest Fo in olivine phenocrysts ($Fo_{91.5}$; *Whattam et al, 2020*) and the highest Fo observed in harzburgite xenoliths from serpentine mud volcanoes recovered by

Expedition 366 in the Mariana forearc ($Fo_{92.5}$; *Shervais and Johnson, 2019*). Samples with MgO <12% are assumed to have undergone net fractional crystallization, whereas samples with MgO >13% are assumed to have undergone net-accumulation of olivine and possibly enstatite.

**Fractionation Modeling**

Fractionation models start with samples calculated to have near primary compositions (i.e., those that have neither fractionated nor accumulated olivine). Fractionation modeling was carried out using Comagmat ver. 3.72 petrologic modeling software (*Ariskin 1999*) using experimentally calibrated equations accounting for the effect of $H_2O$ on crystallization temperatures (*Almeev et al., 2007, 2012*). For selected HSB and LSB primitive compositions (i.e., MgO ~12-13%), equilibrium and fractional crystallization calculations have been performed at constant pressure 200 MPa, considering the accumulation of the partial melts at shallower levels after their extraction from the mantle (see below). The hydrous character of HSB and LSB boninitic glasses (1.3-3.2 wt% $H_2O$, *Reagan et al., 2020*) required the presence of at least 1wt% $H_2O$ in their starting parental melts. All simulations have been carried out along NNO oxygen buffer, bearing in mind the more oxidized nature of the boninitic melts when compared to FABs previously reported in the literature (*Brounce et al., 2015*).

Fractional crystallization of the HSB with 1 wt% melt $H_2O$ (sample 352-U1442A-28R-1-W 0/5, 237.43 mbsf) drives residual melts towards the field of evolved HMAs (Figure 14, purple solid line). Crystallization is initially controlled by olivine (1340°C-1245°C), then by Opx (1240°C-1114°C), and finally by Opx+Cpx+Plag (1240°C-1114°C). Due to the fractional character of crystallization and reaction relationships, Opx crystallizes immediately after Ol, and Cpx after Opx, contradicting natural observation where Ol-Opx, and Opx-Cpx, may coexist in a certain interval of mg# numbers (*Whattam et al., 2020*). In addition, although the calculated fractional crystallization liquid line of descent (LLD) reproduces the natural trend fairly well, it just denotes the lowest $Na_2O$, lowest $Al_2O_3$ and highest $SiO_2$ contents of natural HMA. Equilibrium crystallization modelling conducted on this sample under the same conditions drives melts to less silicic, more aluminous and more sodic compositions when Opx is stabilized. Peritectic reaction between Ol and high $SiO_2$ boninitic melt to produce Opx proceeds within a ~15°C range and is recorded in composition of residual liquids (Figure 14, red solid line). The modelled FeO contents are also closer to their natural counterparts. However, due to continued $H_2O$ enrichment, plagioclase is destabilized at 1063°C although, in natural HSB, plagioclase is present in the groundmass. Therefore, we infer that natural compositional trends are controlled by crystallization when minerals were not effectively fractionated from their parental melts but were partially re-equilibrated to some extent during further evolution and magma ascent.

The same scenario can be also proposed for the crystallization of LSB magmas. As for HSB, fractional crystallization of LSB sample 352-U1439C-20R-3-W 15/18, 341.16 mbsf resulted in an extremely short interval where Ol-Opx and Opx-Cpx can still coexist (Figure 14, blue and red dotted lines respectively). Fractional crystallization of LSB demonstrates a very short temperature interval where Opx was stable. This contradicts petrographic observations of the natural LSB samples where Opx occurs over a wide compositional range. In contrast, equilibrium crystallization models exhibit 30°C and 150°C intervals where Ol and Opx, and Opx and Cpx, could coexist and resolve the problem. In addition, modelled LLD for the case of equilibrium crystallization (red dotted line in Figure 4), turns (when Opx is stabilized) to the highest $Na_2O$, highest $Al_2O_3$ and lowest $SiO_2$ contents of natural HMAs, bracketing the boundary compositions.

In general, the difference between HSB and LSB crystallization is related to the role of low- and high-Ca pyroxenes. HSB is initially located in the primary field of Opx within the basalt tetrahedron, and its crystallization is controlled by Ol, then Ol+Opx, and Opx+Cpx+Plag crystallization. Crystallization of LSB begins with Ol-only crystallization, and is followed by Cpx+Opx and Cpx+Opx+Plag. The range of natural HMA compositions requires several distinct parent magmas in which initial $H_2O$ may vary from 1 to 4% (see below). Each of these parental melts will follow a certain LLD because of the strong control of $H_2O$ on the stability of the fractionating minerals, resulting in a change of crystallization sequences. However experimental study of low pressure crystallization of LSB and HSB is currently lacking.

**Partial Melting**

Boninite melt models are constructed using the approach of *Shervais and Jean (2012)* and *Shervais et al. (2019),* focusing on two groups of samples: those from units >250 mbsf, comprising LSB and HMA, and those from units <250 msbf, largely comprising HSB. For simplicity, we refer to these intervals as *LSB* and *HSB,* respectively, in the following models. Modes and melt proportions for spinel lherzolite are from *Niu (2004).* In spinel-field melting, harzburgite is formed after ~20% melt extraction, while clinopyroxene is completely removed from the source at ~25% melting. All models assume non-modal pooled fractional melting *(e.g., Shaw, 1970; Rollinson, 1995),* with 1% retained melt fraction. A detailed discussion of our melt model parameters, along with distribution coefficients and input compositions, is presented in *Data Supplement DS03.*

Our partial melting models are based on a boninite source mantle that was the refractory residue of earlier partial melting events. Prior source depletion of the mantle wedge is required by the extremely low concentrations of incompatible elements not incorporated significantly into subduction-derived melts, e.g., the HREE and Ti. In contrast, the concentration of other incompatible elements (*e.g.*, LREE, Sr, Pb, Zr, Hf) are too high to come from such a highly-depleted source (e.g., Figure 11). These requirements for the boninite source mantle (highly depleted Ti, HREE, moderately sloping HREE) support the choice of FAB residual mantle as our starting composition. As documented by *Shervais et al. (2019)*, REE concentrations in FAB can only be modeled by a combination of 2-3% garnet-field melt extraction (to achieve the observed MREE-HREE slope) followed by 10-20% spinel field melt extraction (to achieve the observed depletion in HREE). Any hypothetical source constructed for boninite extraction would thus resemble FAB residual mantle. The fact that boninite is sourced from the same mantle wedge region as FAB, after FAB extraction, makes refractory FAB mantle the most likely source. This choice is supported by the highly-depleted peridotites recovered from forearc serpentinite seamounts (*e.g., Parkinson and Pearce, 1998; Fryer et al., 2020*), some of which have old mantle depletion ages based on Os isotopes (*e.g., Savov et al, 2006b*).

Our FAB models used the *"Depleted MORB-source Mantle"* (DMM) of *Salters and Stracke (2004)* as the starting composition (*Shervais et al, 2019*). This composition is similar to the E-DMM of *Workman and Hart (2005)*; the depleted D-DMM of *Workman and Hart (2005)* is approximated by extraction of about 0.3% garnet field melt plus 1.1% spinel field melt from the *Salters and Stracke (2004)* composition. We calculated a FAB residual mantle composition from the DMM of *Salters and Stracke (2004)* by extracting 2% melt in the garnet field and 15-20% melt in the spinel field, with a 1% retained melt fraction (*Shervais et al., 2019, and Data Supplement DS03*).

A second requirement for the boninite source is that it must be re-enriched with incompatible trace elements prior to melting. Simple melting models show that partial melting of highly depleted residual mantle compositions without addition of a fluid or melt component results in melts that are extremely depleted in trace elements, and do not resemble any observed lava compositions. This is because FAB residual mantle is already highly depleted relative to fertile MORB-source mantle, and any melt extracted without prior re-enrichment is too depleted to represent any known terrestrial magmas. Because many of the elements enriched in excess of unfluxed model compositions are melt-mobile only, we infer that the flux component is most likely a hydrous melt phase derived from subducting oceanic lithosphere.

The distinctive chondrite-normalized concentration patterns observed in the axial LSB lavas (positive slope La-Nd, flat to slightly negative slope Sm-Lu, with slight hump at Nd-Sm; Figure 10B-D, F-G) indicate enrichment by melts from an amphibole-rich source. The off-axis HSB upper lavas, in contrast, are LREE-enriched relative to the axial LSB lavas, which requires enrichment with a sediment-derived melt component (Figure 10A, E).

Another constraint is that the slab melt must have a positive Zr-Hf anomaly relative to Nd-Sm to create the observed positive anomalies observed in both the LSB and HSB; this observation is consistent with an amphibolite-facies derived melt flux (*Data Supplement DS03C, D*). The sediment melt component must have similar positive Zr-Hf anomalies, and must be LREE-enriched to offset the LREE-depleted slab melt composition (*Data Supplement DS03C, D*). The total amount of flux to the wedge cannot exceed 2-3% without requiring unreasonably high amounts of subsequent partial melting; smaller total fluxes can be compensated by lower amounts of partial melting, but at very low fractions of melting the overall patterns become difficult to match. The assumed mantle wedge source (residual FAB source) requires ~15-20% melt extraction in order to match the HREE, which changes little during second stage melting.

Input compositions are presented in *Data Supplement DS03*, with representative results in *Data Supplement DS04*. For our slab-derived melt component, we take a 30% melt of the super-composite Site 801 (tholeiite) *altered oceanic crust* (AOC) composition of *Kelley et al., (2003),* leaving an amphibolite residue. We also tested models with higher pressure slab melting (garnet amphibolite and eclogite residue). Garnet-facies melts are LREE-enriched, and cannot reproduce the flat to slightly down-turned LREE patterns observed in LSB. This is shown in a plot of *Sm vs Zr/Sm* that includes models for mantle melts enriched by amphibolite-derived, garnet amphibolite-derived, and eclogite-derived melts; all garnet-facies melts at too high in Sm to match the extremely low concentrations observed in boninite (*Data Supplement Figure DS04B*).

The sediment melt component was modeled using a relatively low-pressure partial melt of GLOSS (global subducting sediment: *Plank and Langmuir, 1998).* We used the melting experiments of *Hermann and Rubatto (2009)* at 2.5 GPa, 750-800ºC (C-1846, C-2446) scaled to the GLOSS composition for our sediment component (*Data Supplement DS03)*.

Critical characteristics of LSB trace element compositions that indicate a match include the slight depletion in LREE (La-Pr) relative to the middle REE (convex pattern), the flat to slight negative MREE-HREE patterns, the strongly negative Nb anomaly, and the distinct positive Zr-Hf anomaly relative to the adjacent REE (Figure 15A, B). LSB may be modelled successfully by fluxing a residual FAB source with 2% melt derived from AOC, followed by 15-20% melting in

the spinel peridotite facies. The model melts match the range of observed compositions across a wide spectrum of incompatible element concentrations (Figure 15A, B). Models using a less depleted FAB residue (15% prior melt extraction) require higher degrees of melting compared with models using a more depleted FAB residue.

Critical characteristics of HSB trace element compositions that indicate a match include the spoon-shaped (concave-upward) REE patterns, enriched LREE concentrations, strongly depleted (negative) Nb anomaly, the distinct positive Zr-Hf anomaly relative to the adjacent REE, and the distinct negative Ti anomaly (Figure 15C, D). The most successful matches between modeled and actual HSB compositions involve fluxing a residual FAB source with ~1-2% slab-derived melt (AOC) plus ~1% melt derived from subducted sediment, followed by ~10% melting in the spinel peridotite facies (Figure 15C, D). Fluid-mobile elements such as Pb and Sr in the HSB typically exceed the enrichments due to the addition of slab+sediment melt, and may require an additional flux of aqueous fluids.

An alternative potential source for off-axis HSB is mantle residual to LSB melt extraction. This model is suggested by the low $TiO_2$ in HSB relative to LSB (e.g., Figure 3B, C), consistent with a more refractory source for HSB. It is supported by the observation that HSB off-axis lavas form after axial LSB lavas, and thus refractory mantle after LSB extraction would be physically present in the future HSB source region. Assuming a source composition of LSB residue after 15% melt extraction, with 1% retained melt, successful matches are obtained with 1% to 1.5% slab-derived melt (AOC) plus ~1% to 0.5% melt derived from subducted sediment, followed by ~10-15% melting in the spinel peridotite facies (Figure 15E, F). The constraints on slab + sediment melt components are relatively tight: the slab component cannot exceed ~2%, nor the sediment melt exceed ~1%, and still achieve a reasonable fit to the data. We suggest that the actual source for HSB is likely to involve a mixture of both FAB residue and LSB residue, such that the models presented here are end members that bracket the actual melting process.

The models presented above are supported by radiogenic Sr-Nd-Hf-Pb isotope data for Expedition 352 samples presented by *Li et al. (2019).* Their data require that the depleted mantle source for LSB was enriched by melt derived from altered oceanic crust in the amphibolite facies, and that the HSB source was enriched by melt derived from altered oceanic crust (AOC) and a pelagic sediment component. These requirements are consistent with the trace element systematics, which document elevated Zr/Sm and La/Sm ratios in boninite that cannot be caused by a simple aqueous flux. However, the excess of some fluid-mobile elements such as Pb and Sr typically exceeds the enrichments calculated by the addition of slab±sediment-derived melt, and seems to require an additional flux of aqueous fluids that may precede melting.

Because there is a large range in potential slab and sediment melt components, these models are not definitive, but they do place significant constraints on the processes involved. The amount of prior melt depletion of the mantle source is relatively robust at 15-20% spinel facies melting after 1-3% garnet field melting. Minor garnet-field melting is required to depress the LREE relative to the HREE, and a minimum of 15% spinel field melting (generally closer to 20% prior melting) is required to lower HREE concentrations in the refractory residue to levels that can reproduce those observed in boninite lavas. Further, the flux of slab- and sediment-derived melt fractions to the residual mantle cannot exceed about 3% without causing enrichments in subsequent melts that exceed observed boninite compositions for any reasonable degree of melting (<25% partial melting). Finally, the flux of sediment- and slab-derived melt cannot be less than about 1% because the low degree of subsequent melting required makes it difficult to match the observed lava compositions. These constraints will remain relatively consistent for most proposed flux compositions.

**Thermobarometry**

Estimates of the pressure and temperature of the magma source were calculated using the method of *Lee et al. (2009)* on the basis of major element composition of the HSB and LSB, in particular, the activity of silica. *Lee et al. (2009)* calculate the primary melt composition by adding or subtracting olivine from the magma composition until the magma Mg# is in equilibrium with a specified source olivine composition. Residual mantle olivine of Fo92 is used here, based on highest Fo olivine in the phenocrysts (*Whattam et al., 2020*); a higher residual olivine Fo would result in higher calculated primary magma MgO contents (*e.g., Parkinson and Pearce, 1998,* found harzburgite olivines as high as Fo93 in the IBM forearc). Plots of the final mass of magma relative to the original mass imply a parent melt composition with MgO ~12-13±1 wt%. Boninite samples with MgO <12 wt% are fractionated relative to the inferred parent melt, whereas samples with MgO >13 wt% have accumulated olivine ± enstatite. Using this measure, approximately two-thirds of the boninites analyzed here have >13 wt% MgO and are thus partial cumulates. This implies that boninites often erupt through crystal mushes and must have transit times to vent that are rapid compared to the Stokes settling velocity of the phenocrysts.

The calculations to determine P and T were performed for primitive magmas with >8% MgO, i.e., boninite (*Data Supplement Table DS05;* Figure 16), with $Fe^{3+}$/Fe-total ratio of 0.21 (Brounce et al., 2015). We tested scenarios for dry melting as well as wet melting with 3-5% $H_2O$ in the primary magma based on water contents measured in IBM boninite glasses (*e.g., Dobson and O'Neil, 1987; Coulthard et al., 2020*); this is supported by the Ca-in-olivine hygrometer results of *Whattam et al. (2020*), which imply 2-4 wt% water in the primary magma. Equilibration

temperatures are highest for dry melting (~1340±60ºC) and lowest for water contents of 5 wt% (~1210±20ºC), all at low pressures (0.3-1.0 GPa dry to 0.46-0.93 GPa wet) relative to MORB and forearc basalts (*e.g., Lee et al., 2009; Perrin et al., 2016; Shervais et al., 2019*). Our preferred water content of 3 wt% results in intermediate temperatures and pressures (~1255±25ºC, ~0.37-0.87 GPa; Figure 16). Pressure variations are on the order of the estimated uncertainty of the barometer (±0.2 GPa; *Lee et al. 2009*), whereas temperature variations between dry and 5% water in melt are greater than the estimated uncertainty of the thermometer (±30-50ºC; *Lee et al. 2009).* Nevertheless, all samples lie within a narrow range of pressure for all models, and temperatures vary over a narrow range (≤50ºC) that are similar to those calculated by mineral-melt equilibria (*Whattam et al., 2020*) for reasonable water contents. These data imply that the boninite melts separated from their source region at extremely low pressures, with LSB melts equilibrating at slightly higher pressures than the subsequent HSB melts (Figure 16; *Data Supplement Table DS05*).

Forearc basalts from Expedition 352 have higher equilibrium temperatures and pressures, forming an array approximately parallel to the dry peridotite solidus (Figure 16; Shervais et al, 2019). The lowest calculated pressures for FAB (~1.2 GPa) are higher than the highest pressures calculated here for boninite (~0.9 GPa), consistent with progressive melting of mantle trapped in the wedge (*Reagan et al., 2017*), where that trapped mantle melts at progressively shallower pressures from FAB to LSB to HSB. In contrast, rear-arc basalts sampled by Expedition 351 (Hole U1438; *Hickey-Vargas et al., 2018*) overlap the P-T array of FAB, but extend to much lower pressures (~0.7 GPa) that overlap the pressures calculated for boninite melting (Figure 16). Their results reflect continued decompression melting in the absence of slab-derived fluids.

Our findings are broadly consistent with the evaluation of *Pearce and Reagan (2019)* based on compiled $SiO_2$-MgO-$TiO_2$ data from published melting experiments. These experiments show that boninite genesis by mantle melting is favored at low pressures from a mantle that had undergone significant prior depletion (*Pearce and Reagan, 2019*). LSB (including our BB subtype) are generated from mantle sources with residual clinopyroxene. Continuous melting of this mantle past clinopyroxene exhaustion produces magmas generated both during clinopyroxene-saturated and clinopyroxene-undersaturated melting. LSB are the integrated melts across most or all of this melting interval. In contrast, the mantle sources for HSB are harzburgite, and the integrated melts are generated from mantle with very little clinopyroxene, resulting in a predominance of cpx-undersaturated melts. Such extreme degrees of melting require a water flux in the modern Earth (*Pearce and Reagan, 2019*).

## DISCUSSION

The magmatic response to subduction initiation in the western Pacific at c. 52.5 Ma was forearc basalt (FAB) followed by boninite suite lavas (*Reagan et al., 2019*). In Part One of our publication of Expedition 352 post-cruise geochemical results (*Shervais et al, 2019*), we detailed the petrogenesis of FAB in two sections cored near the trench. Here we examine the implications of geochemical record of the two continuous cores of boninite and boninite series drilled upslope at Sites U1439 and U1442.

### Axial versus Off-axis Volcanism

Chemostratigraphic profiles at both boninite sites are marked by major discontinuities in their major and trace element characteristics at ~250 mbsf (Figures 12, 13), which represent the transition from dominantly LSB+HMA volcanism below (deeper than) 250 mbsf to dominantly HSB volcanism above (shallower than) 250 mbsf. In addition, lavas above 250 mbsf are isotopically distinct from the lower lavas, with lower $\varepsilon Nd_i$, $\varepsilon Hf_i$ and higher $^{206}Pb/^{204}Pb$ (*Li et al., 2019*). These characteristics require distinct source compositions for lavas above and below 250 mbsf, despite their close spatial and temporal association. The deepest unit in U1439C (Unit 10) comprises coarse-grained diabase and finer-grained dikes, interpreted by the shipboard scientists (*e.g. Reagan et al., 2017*) to represent the top of a dike complex consanguineous in part with overlying lavas below 250 mbsf.

Chemostratigraphic units >250 mbsf are interpreted to form at a forearc spreading axis during this initial stage of rapid spreading, succeeding slightly older FAB lavas (*e.g., Reagan et al., 2017, 2019; Li et al, 2019; Shervais et al, 2019*). Subsequent upper lavas (<250 mbsf) are interpreted to have formed off-axis, as a precursor to extensive boninite volcanism that formed the Bonin Ridge. Tectonic models for this progression (*Reagan et al. 2019; Li et al., 2019*) are consistent with geodynamic models of subduction initiation, which show extensive, rapid, and near-trench seafloor spreading with accompanying development of basaltic to boninitic oceanic crust in response to slab roll-back (*e.g., Hall et al., 2003; Leng et al., 2012; Maunder et al., 2020*). Critically, the lack of a sediment component in the axial lavas (>250 mbsf) implies that the subducting sediments were accreted during the earliest stage of subduction. Indeed, recent geodynamic models specifically designed to recreate the spatial, temporal and compositional sequence of magmatism observed from Expedition 352 predict that sediments are initially scraped off the slab (*Maunder et al., 2020*). Sediment melts only become important in the off-axis lavas (<250 mbsf), leading to the formation of the classic spoon-shaped REE patterns that are also characteristic of Chichijima boninite.

**Subduction Initiation and Boninite Petrogenesis**

The formation of boninite is intimately tied to the formation of FAB by decompression melting at relatively high T-P conditions (>1380ºC, 1.3-2.3 GPa), as the formation of a depleted refractory residue is a necessary precursor to boninite formation (*Pearce and Reagan, 2019)*. The data presented here are consistent with the petrogenesis of boninite magmas by fluid-enhanced melting of this previously depleted mantle, and further document the involvement of partial melts derived from the subducting slab (altered oceanic crust) and its sedimentary cover. The association of boninite with incipient subduction implies that the required enrichment of the mantle source region could only come from the addition of a melt fraction derived from the subducting slab (*e.g.*, Figure 9B). Systematic changes in the chemostratigraphy of the core further show that this slab-derived component changed with time, from partial melts of altered oceanic crust in the amphibolite facies initially to partial melts of altered oceanic crust plus abyssal sediment, as documented by trace element modeling presented here, and supported by the radiogenic isotope data of Li et al (2019). This process has been modeled numerically by *Maunder et al (2020).*

A major finding of this study is that the earliest boninite suite lavas (LSB) are characterized by relatively flat chondrite-normalized MREE-HREE patterns with distinct LREE-depletion ($La_{ch}/Sm_{ch}$ <1.0) and modest positive Zr/Sm anomalies. These characteristics require a slab melt component derived from partial melting of amphibolite-facies altered oceanic crust; garnet amphibolite or eclogite-facies melting is ruled out by their low Sm concentrations *(e.g, Figure DS04B*). These early boninite suite lavas are distinct from the off-axis HSB suite and from the classic boninites of Chichijima (*e.g. Dobson et al, 2006*), which are characterized by concave-upward REE patterns ("U-shaped" or "spoon-shaped") and larger positive Zr/Sm anomalies. These "off-axis" HSB lavas require a source enriched by melt derived from subducting sediment as well as melt derived from amphibolite-facies altered ocean crust (e.g., *Pearce et al., 1992*).

Boninite series magmas form from the FAB refractory residue at slightly lower pressures, after the newly sinking slab of oceanic crust begins to dewater and melt. The rapid continuous spreading in the nascent forearc allows the FAB residue to rise adiabatically to relatively shallow depths, where hydrous slab-derived melts enrich the depleted residue and lower its solidus, allowing the production of "second-stage" melts to form boninite.

Assuming an average Pacific Plate subduction rate of 50 mm per year (*e.g., Fryer, 1996; Fryer et al., 1990; Stern et al., 2003; Faccenna et al., 2009, 2018; Gong et al., 2018; Kong et al., 2018; Kurz et al., 2019*) and an initial subduction angle in the range of 30° along the northern Izu-Bonin subduction segment, as indicated by seismic tomography (*e.g., Jaxybulatov et al., 2013; Gong et al., 2018; Kong et al., 2018*), subduction will bring the tip of the subducting Pacific Plate to ~50

km depth, and therefore amphibolite facies metamorphic conditions, within ~2 Ma (*e.g., Ringwood, 1974, 1977; Chapman et al., 2019*) after subduction initiation. Allowing about ≤1 Ma of non-magmatic spreading during the first phase of subduction initiation, this matches the circa 0.7 Ma transition from early proto-forearc spreading (FAB), related to upwelling asthenosphere, to late proto-forearc spreading (boninite) magmatism described by *Reagan et al. (2019)* and *Shervais et al. (2019).* Geodynamic modeling of subduction initiation along a transform fault has replicated the thermal conditions needed for slab melting in the amphibolite facies, the progression of FAB to boninite lavas, and the timescales over which these events occur during initiation of the Bonin arc (*Maunder et al., 2020*).

As discussed above, the addition of slab-derived melts to the refractory mantle wedge is key to the formation of boninite. One critical aspect of this model is that sediment-derived melts do not contribute to the axial lavas, but are required to form the off-axis lavas. The removal of sediment from the earliest subducting plate most likely occurred prior to foundering of the slab, perhaps during an initial phase of convergence between the upper plate and future lower plate (*e.g., Hall et al, 2003; Gurnis et al., 2004; Leng et al., 2012).* Alternatively, delayed sediment subduction may occur in response to the physical properties of cold abyssal sediment *(Maunder et al. 2020*).

The interpreted progression of subduction initiation magmatism is shown in Figure 17. This shows schematically a potential early phase of plate convergence, which denudes the leading edge of the future upper plate by thrusting and essentially doubles the thickness of sediment away from the tip of the slab. This denudation is implied by the lack of a sediment component in the older LSB lavas. Once the lower plate begins to founder, the denuded oceanic crust of the leading edge is heated progressively for 1-2 Myr until it begins to melt under amphibolite facies conditions. This stage 1 melt fluxes the refractory residue from FAB genesis, which undergoes renewed melting to form the axial boninite series, comprising large LSB and HMA. As foundering continues, the accreted sediment joins altered oceanic crust in the melt window, forming stage 2 melts that flux the refractory wedge of FAB residue. This in turn leads to off-axis volcanism comprising largely boninite of HSB composition.

The observations of magma mingling and magma mixing, both physically in the core (*e.g.,* Figure 5) and chemically in the chemostratigraphy (Figures 12 and 13), document a dynamic magmatic environment in which multiple magma reservoirs exist simultaneously, and which may or may not interact with one another prior to eruption. These magma reservoirs must also be ephemeral, as mixed magma horizons are often overlain by lavas which carry no indication of mixing, or by lavas with distinctly different compositions indicative of having by-passed the

magma reservoir that sourced the underlying mixed lavas. The ubiquity of this dynamic magmatic system implies that magmatic stratigraphy may change rapidly along strike as well as vertically in individual sections.

**Subduction initiation and ophiolites**

After considerable controversy, the link between supra-subduction zone (SSZ) ophiolites and lithosphere generation during subduction initiation is now well-established (e.g., *Miyashiro, 1973; Pearce et al, 1984; Stern and Bloomer 1992; Shervais, 1990, 2001; Metcalf and Shervais, 2008; Reagan et al., 2010*). Rocks recovered on Expedition 352 document the foundering and subsequent roll-back of oceanic crust driving early decompression melting to form FAB and subsequent melt-fluxed melting of the refractory mantle (FAB residue) to form boninite and related rocks. This sequence is also observed in some modern subduction initiation settings (*e.g.*, Matthew-Hunter system: *Patriat et al, 2019*). Many SSZ ophiolites have a consistent magmatic progression, especially as documented in the plutonic sections (*Shervais, 2001*), although in some ophiolites FAB are absent and instead replaced by arc tholeiites formed by fluid-fluxed melting (no slab melt component; *e.g.*, Coast Range Ophiolite, California; *Shervais et al, 2005*). The magmatic progression consists of early FAB or arc tholeiite, layered gabbro, which is intruded wehrlite, pyroxenite, and primitive gabbro derived from boninite suite magmas, and may be followed by diorite-tonalite intrusions (*e.g., Shervais et al., 2005; Shervais, 2008*). Similar relations have been documented in the Semail Nappe of Oman (*Adachi and Miyashita, 2003; Ishikawa et al, 2002; MacLeod et al, 2013; Tamura and Arai, 2006; Python and Ceuleneer, 2003*) and the Troodos Massif of Cyprus *(e.g., Cameron, 1985; Benn and Laurent, 1987; Sobolev et al, 1993; Woelki et al., 2018, 2019, 2020*).

It would be a mistake, however, to apply subduction initiation in the IBM system to all ophiolites. The IBM system represents an endmember to a spectrum of potential tectonic analogues: it formed far from any continental influence where extremely old ocean crust foundered adjacent to extremely young ocean crust (Philippine Sea plate). The Philippine Sea plate itself was sourced from mantle that had experienced prior melt depletion, causing FAB and rear arc lavas to be more depleted than normal MORB, and there was possible influence from the Manus hotspot (*Shervais et al., 2019; Yogodzinski et al., 2018*). This confluence of factors may apply to some SSZ ophiolites, but others likely formed under somewhat different circumstances, *e.g.*, closer to continental margins, foundering of relatively younger ocean crust, intersections of back-arc basins with trenches (Northern Lau Basin; *Resing et al., 2011*), forearc rifting (SEMFR; *Ribeiro et al. 2013*), and normal MORB asthenosphere in the upper plate. These factors will influence the exact

nature of the magmatic response, although the relative sequence of tectonic events and magma types will commonly remain the same.

In addition, the dominance of LSB lavas in U1439C and U1442A, which typically lack the upward-concave REE patterns of "classic" boninite, implies that boninite lavas in ophiolites may be misidentified if the major element compositions are too altered for formal classification. In such a case, the similarity of LSB REE patterns to MORB demonstrates that REE pattern shape should not be used as the only indicator of ophiolite tectonic setting.

## CONCLUSIONS

The magmatic response to subduction initiation at the IBM convergent margin, detailed here and in related publications (*Shervais et al., 2019; Reagan et al., 2019; Li et al., 2019; Maunder et al., 2020; Whattam et al., 2020*), documents a more complex and nuanced process than has been proposed previously. The initial stage of decompression melting to create forearc basalt (FAB) resembles MORB formation at divergent plate boundaries (*e.g., Reagan et al., 2010*), but the extent of melting is commonly higher (up to 20% melt extraction) and the trace element compositions more varied (*Shervais et al., 2019*). This represents in part the effects of a prior melt depletion event that affected the mantle beneath the entire proto-Philippine Sea plate (*Yogodzinski et al., 2018; Hickey-Vargas et al., 2018*) and in part higher mantle potential temperatures potentially associated with the Manus hotspot during the earliest stages of subduction initiation (*Shervais et al., 2019*). Most FAB formed at a spreading axis in response to rapid seafloor spreading above the sinking Pacific plate margin, but the uppermost FAB crust formed by off-axis volcanism, possibly coincident with the onset of axial boninite volcanism (*Li et al., 2019; Reagan et al., 2019; Shervais et al., 2019*).

The onset of boninite volcanism at the axial spreading center is marked by dominance of low-silica boninite (LSB) and high-Mg andesite (HMA). The inference that the early LSB/HMA suite formed at an axial spreading center is based on their occurrence in a sheeted complex at the base of U1439C (*Reagan et al, 2017*). Modeling of less incompatible trace elements shows that the mantle source was strongly depleted relative to DMM and we infer that the boninite source was residual to FAB melt extraction (*e.g., Reagan et al, 2017*). In contrast, the more highly incompatible trace elements do not reflect this depletion, requiring source enrichment prior to melting. The trace element data *(e.g.,* elevated Sr8 and Zr/Sm ratios; Figures 3, 9) and modeling presented here show that the source of enrichment in the LSB/HMA suite of axial lavas was a hydrous melt derived from partial melting of oceanic crust under amphibolite-facies conditions. This conclusion is supported by the isotopic data of *Li et al.* (*2019*). The lack of a sediment

component (shown by lack of LREE enrichment in LSB) indicates oceanic sediments may have been accreted at shallow depths in during the earliest stages of subduction.

A key aspect of the axial LSB/HMA suite is their trace element signature, which is marked by relatively flat MREE-HREE chondrite normalized patterns with a distinct depletion in the LREE ($La_{ch}/Sm_{ch}$ <1). This signature is not generally associated with boninite lavas, which are commonly assumed to have concave "U-shaped" REE patterns. These axial LSB/HMA lavas dominate the recovered core (81% of U1439C, 62% of U1442A), and may be equally dominant in paleo-forearc settings (SSZ ophiolites).

The uppermost boninite suite lavas are high-silica boninite (HSB), which are inferred to have formed by off-axis volcanism. The HSB suite is characterized by the classic "U-shaped" REE patterns associated with boninite lavas, and is broadly similar to boninite suite lavas exposed west of the drill sites on Chichijima and the Bonin Ridge (*e.g., Umino, 1986; Dobson et al, 2006*). These lavas represent the culmination of subduction initiation magmatism, forming shortly before the onset of stable arc volcanism (*Ishizuka et al., 2011a, 2020*), but are far less common than the underlying LSB/HMA suite lavas on the trench slope. In contrast, HSB suite lavas may dominate under the Bonin Ridge, which represents an incipient proto-arc formed prior to the onset of stable subduction (*Reagan et al, 2019*). The trace element data presented here show that these HSB off-axis lavas require a sediment melt component in addition to melt derived from altered oceanic crust.

All of the boninite suite magmas last equilibrated with their mantle source at relatively low pressures (0.4 to 0.9 GPa), with HSB melts having equilibrated at slightly lower pressures than LSB melts. In contrast, FAB melts locally equilibrated at ~1.2-1.6 GPa (*Shervais et al, 2019*), although some FAB-like rear-arc basalts of the Amami-Sankaku basin equilibrated at pressures similar to boninite (~0.6-1.3 GPa: *Hickey-Vargas et al, 2018*). This progression of decreasing pressure in the order FAB>LSB>HSB is consistent with progressive shallowing of mantle trapped in the wedge, with melting caused by continual fluxing of slab-derived fluids and melts. The change from LSB to HSB reflects a change in both the composition of the slab melt input to a refractory FAB residue and the reduction of clinopyroxene in the source mantle.

Finally, the common occurrence of magma mingling and magma mixing between more- and less evolved melts, observed within and between igneous units in each core, documents a dynamic magma system with multiple small shallow magma reservoirs that overlap in space and time, sometimes erupting simultaneously to form mingled lavas and sometimes intersecting to mix or partially mix.

*Acknowledgements: This research used samples and/or data provided by the International Ocean Discovery Program (IODP). The authors are grateful for support from IODP, the JOIDES Resolution Facility, and the scientific staff and crew aboard the JOIDES Resolution during Expedition 352. Funding support to U.S. participants (*JWS, MKR, JGR, WN*) from the Consortium for Ocean Leadership and from the National Science Foundation is gratefully acknowledged (OCE-1558689 to Shervais; OCE-1558647 to Reagan, OCE-1558855 to Ryan, and OCE-1558608 to Nelson). Prytulak was supported by NERC directed grant NE/M010643/1. Chapman was supported by the Australia-New Zealand IODP consortium and the ARC LIEF scheme (LE140100047). Almeev was supported by the German Science Foundation (DFG, Project AL1189/8-1). Pearce was supported by NERC (UK) grant (NE/M012034/1). Kurz appreciates support by the Austrian Academy of Sciences and funding by the Austrian Science Fund (FWF Project P27982-N29). Kirchenbaur appreciates funding by the German IODP consortium and the BGR Germany. All data submitted to the Pangaea database for archiving. We thank Ivan Savov, Marcel Regelous, and two anonymous reviewers for their thorough and thoughtful reviews, which markedly improved the manuscript. All analytical data are archived in the Pangaea database: https://doi.pangaea.de/10.1594/PANGAEA.921304.*

**Figure Captions**

**Figure 1.** Location maps for IODP Expedition 352. (A) The Izu-Bonin-Mariana arc system along the western Pacific margin, and the Philippine Sea plate back-arc basins. Red triangles show location of the Expedition 352 drill sites; Yellow circles show drill sites for sister expeditions 350 *("Rear Arc")* and 351 *("Arc Origins").* MT = Mariana Trough; KPR = Kyushu-Palau Ridge; PVB = Parece-Vela Basin; WPB = West Philippine Basin, SB = Shikoku Basin, Amami Plateau; ASB = Amami Sankaku Basin; DR = Daito Ridge; ODR = Oki-Daito Rise. Dashed inset show area of figure 1B. (B) Detail of the Bonin arc segment, showing arc volcanoes on the left (West), the Izu-Bonin trench on the right (East), with the Ogasawara Plateau with the islands Mukojima, Chichijima, and Hahajima. U1440 and U1441 are closest to the trench, whereas U1439 and U1442 are farther upslope. Inset shows area of Figure 1C. (C) Detail topographic map of the inner trench wall showing drill site locations for U1439, U1440, U1441 and U1442. Map colors: Purple = ultramafic rocks; Blues = plutonic rocks (gabbros, dolerites); Greens = Forearc Basalt; Yellow-greens = boninites, and yellow-orange = andesites. Figures 1A and 1B created with GeoMapApp. Figure 1C from *Reagan et al, 2015a*.

**Figure 2.** Lithologic columns for holes (A) U1439C and (B) U1442A, modified from Reagan et al., (2015). Columns show depths (meters below seafloor), core number (R = rotary core barrel), recovery for each core (black bars, thickness proportional to recovery), lithologic log, formal Unit number, and brief description. Hatched red bars adjacent to lithology column represent fault zones. Upper lavas (off-axis, see text) include units 1-4 in U1439C and unit 1 in U1442A. Axial volcanic units all deeper than 250 mbsf.

**Figure 3.** Boninite suite classification diagrams showing samples from sites U1439 and U1442 after correction for secondary calcite and hydration. Forearc basalts from sites U1440 and U1441 shown for comparison. (A) $SiO_2$ vs MgO modified after Pearce and Reagan (2019), showing fields for HSB and LSB; the LSB field is modified to show the subset of "basaltic boninite" (BB) identified during Expedition 352 (Reagan et al., 2017). (B) MgO vs $TiO_2$ after Pearce and Reagan (2019). LSB/BB are generally higher in $TiO_2$ than HSB at given MgO; (C) $SiO_2$ vs $TiO_2$, showing distinct trends for BB, LSB, and HSB. HSB: high-silica boninite, LSB: low-silica boninite, BB: basaltic boninite,

**Figure 4. (A)** The Si8-Ti8 classification diagram of Pearce and Reagan (2019). Expedition 352 samples all project to $TiO_2$ <0.5% at 8% MgO; silica at 8% MgO spans basalt, basaltic andesite, andesite and dacite. Altered boninite have lost silica and plot just inside the low-Ti (LoTi) basalt field. Most forearc basalts have Si8 <52% and Ti8 ~1%, similar to the depleted end of the MORB array (gray) in the *Basalt-Andesite-Dacite-Rhyolite* (BADR) field. One FAB andesite has high silica and $TiO_2$, plotting in the *Siliceous High-Mg Basalt* (SHMB) field. (B) Ti8-Sr8 diagram, showing the mantle depletion trend of oceanic basalts, in contrast to boninite series lavas, which are extremely low in Ti8 (prior melt extraction) but strongly enriched in Sr8 due to slab-derived partial melts. FAB: Shervais et al. (2019); Oceanic basalts: Jenner and O'Neill (2012).

**Figure 5.** Macroscopic photographs of core from holes U1439C and U1442A. A-C: Magma-mingling textures in U1439C, Unit 8. (A) mingling of light-colored HMA with dark LSB (*U1439C, 31R3 58-73*); (B) chilled margin contact of low-Cr HMA with high-Cr LSB (*U1439C, 29R1 19-28*); (C) mingling of light-colored HMA with dark LSB (U1439C, 31R1 19-31); (D) cuspate contact between two HSB magmas with similar Cr concentrations: dark lava more crystalline, light lava has glass chilled margin about 5 mm thick with less glassy interior (*U1442A, 24R1 138-143*); approximate location of TS195 shown as dashed rectangle; (E) macro image of thin section TS195, showing cuspate contact between two HSB lavas; see Figure 7GH for photomicrograph (*U1442A, 24R1 TS195*); (F) hyaloclastite breccia with boninite pumice clasts U1442A Unit 1c (*U1442A, 19R1 10-20*).

**Figure 6.** Phenocryst abundances in (A) U1439C and (B) U1442A, as well as groundmass plagioclase content, modified from Reagan et al. (2015). Olivine and enstatite are dominant phases in HSB (upper lavas), olivine is the dominant phenocryst (±enstatite, ±augite) in LSB; BB lavas are characterized by olivine-enstatite-augite assemblages. Plagioclase is found as phenocryst in andesite (+augite) and in many HMA, which may also contain groundmass plagioclase. Hatched red bars adjacent to lithology column represent fault zones.

**Figure 7.** Photomicrographs of select samples; all bar scales = 1 mm. (A,B) Plane light (UPL) and crossed polar (UXN) images of typical HSB lava; abundant mm-scale phenocrysts of olivine and bronzite in glassy groundmass with abundant needles of low-Ca pyroxene (*U1442A, 12R1, TS190)*; (C,D) Close-up images (UPL, UXN) of HSB lava showing pale glass matrix with large olivine phenocryst and smaller bronzite and olivine grains (*U1439C, 2R1, TS77)*; (E,F) HSB lava showing pale glass matrix with microlites of bronzite and larger olivine and bronzite phenocrysts (*U1439C, 2R1, TS77)*; (G,H) Magma-mingling contact in thin section TS195, UPL and UXN; quenched glass margin on right with olivine and bronzite phenocrysts, coarser crystalline lava with similar phenocrysts on the left; see Figure 5DE for macroscopic images (*U1442A, 24R1, TS195)*; (I) LSB lava with phenocrysts of olivine in matrix of glass with abundant microlites of bronzite, UXN (*U1439C, 27R3, TS125*); (J) LSB lava with large mm-scale olivine phenocrysts containing melt inclusions, UXN (*U1439C, 27R3, TS126*); (K,L) Micro-dolerite LSB with intersertal texture comprising bronzite microlites and small olivine crystals (*U1439C, 41R1, TS154*); (M,N) Basaltic boninite small olivine and augite phenocrysts in glassy matrix with bronzite microlites; note two aphyric glass inclusions (*U14442A, 30R3, TS204*); (O,P) High-Mg andesite with phenocrysts of augite and plagioclase in glassy matrix with abundant bronzite microlites (*U14442A, 40R1, TS215*).

**Figure 8**. MgO-variation diagrams for U1439 and U1442 boninite series lavas, compared to forearc basalts and mid-ocean ridge basalts (grey symbols). MgO weight percent oxide (x-axis) versus (A) FeO*, (B) Zr µg/g, (C) Y µg/g, (D) Sm µg/g, (E) Yb µg/g,and (F) Sr µg/g. Expedition 352 boninite series lavas show iron depletion with decreasing MgO, and extremely low Zr, Y, Sm and Yb relative to MORB. Expedition 352 FAB Zr overlaps boninite, but FeO*, Y, Sm, and Yb overlap the MORB field. FAB Sr concentrations are lower than MORB, but boninite Sr overlaps the MORB field, suggesting a slab melt component.

**Figure 9.** Trace element ratio plots compared to FAB and MORB. (A) Ti-V. Ti and V concentrations are extremely low in boninite (Ti <3000 µg/g, V <220 µg/g), and higher in FAB (>3000 µg/g, V >240 µg/g), while normal MORB have Ti/V ~20-50 (Shervais, 1982). Yellow circles = U1438 basalts (Hickey-Vargas et al., 2018). (B) Zr/Sm vs Sm. MORB follows normal melt depletion trends (slight decrease in Zr/Sm with decreasing Sm), whereas FAB show the effects of prior melt depletion (Zr/Sm <20 at Sm <3 µg/g). In contrast, boninite suite lavas show progressively increasing Zr/Sm (25 to 70) at relatively constant low Sm concentration (<1.5 µg/g). Almost all boninites exceed the MORB Zr/Sm ~28.1 (Sun and McDonough, 1989). This upward enrichment trend is interpreted to result from addition of slab melt components to the refractory boninite source.

**Figure 10.** Chondrite-normalized (C1 chondrite of Sun and McDonough, 1989) rare earth element concentrations in boninite suite lavas. (A-D) U1439, (E-G) U1442. (A) U1439 Units 1-4, 180-250 mbsf; (B) U1439 Units 5-6 250-389 mbsf, (C) U1439 Units 7-8 390-470 mbsf, (D) U1439 Units 9-10 485-541 mbsf, (E) U1442 Unit 1 82-238 mbsf, (F) U1442 Unit 2 258-385 mbsf, and (G) U1442 Units 3-4 400-522 mbsf.

**Figure 11.** MORB-normalized (Sun and McDonough, 1989) multi-element variation (spider) plots of boninite suite lavas. (A-D) U1439, (E-G) U1442. (A) U1439 Units 1-4, 180-250 mbsf; (B) U1439 Units 5-6 250-389 mbsf, (C) U1439 Units 7-8 390-470 mbsf, (D) U1439 Units 9-10 485-541 mbsf, (E) U1442 Unit 1 82-238 mbsf, (F) U1442 Unit 2 258-385 mbsf, and (G) U1442 Units 3-4 400-522 mbsf.

**Figure 12.** Chemical stratigraphy of hole U1439C. (A) $TiO_2$ wt%, (B) Ti/V ratio, (C) Ti/Zr ratio, (D) Zr/Sm ratio, (E) La/Sm ratio. Horizontal dashed line = axial vs off-axis transition; vertical dashed line is approximate break between axial and off-axis lavas in Ti/V and La/Sm ratios. See text for discussion.

**Figure 13.** Chemical stratigraphy of hole U1442A. (A) $TiO_2$ wt%, (B) Ti/V ratio, (C) Ti/Zr ratio, (D) Zr/Sm ratio, (E) La/Sm ratio.Horizontal dashed line = axial vs off-axis transition; vertical dashed line is approximate break between axial and off-axis lavas in Ti/V and La/Sm ratios. See text for discussion.

**Figure 14.** Forward modeling of BON fractionation trends from Comagmat (*Ariskin 1999; Almeev et al, 2007, 2012*). Paths are shown for equilibrium crystallization (red lines) and fractional crystallization (purple lines), for both a representative HSB (solid lines) and LSB (dotted lines). All assume 1% $H_2O$ at 200 MPa. Whole rock and glass compositions shown for comparison. See text for details.

**Figure 15.** Rare earth and multi-element melt models for (A, B) LSB (>250 mbsf), (C, D) HSB (<250 mbsf) with FAB residual source and (D, E) HSB (<250 mbsf) with an LSB residual source. REE normalized to C1 chondrite of Sun and McDonough (1989); multi-element plot normalized to NMORB of Sun and McDonough (1989). Pooled fractional melting with 1% retained melt fraction. LSB source is assumed to be residue of FAB melting (20% melting) plus slab melt of altered oceanic crust (5% and 30% melting in the amphibolite facies). HSB source is assumed to be FAB residue after 20% melt extraction, plus slab and sediment melts, or the residue of LSB melting after 15% melt extraction, with 1% retained

melt plus slab and sediment melts. Filled symbols are model results, open symbols are representative samples. See text and supporting documents DS04A and DS04B for details.

**Figure 16.** Thermobarometry of Expedition 352 boninite, using method of Lee et al. (2009). Calculated on the basis of Fo92 refractory mantle, dry and with 3% and 5% water content. PT arrays for FAB (*Shervais et al, 2019*) and rear-arc basalts of Expedition 351 (*Hickey-Vargas et al, 2018*) shown for comparison, along with dry peridotite solidus. Measured water content in boninite glass is ~2wt%; vesiculation indicates that this is minimum value. Higher water contents lower the equilibration temperature ~15ºC/wt% water and increases pressure slightly. See text for discussion.

**Figure 17.** Schematic model for the origin of boninite during subduction initiation in the Iz-Bonin forearc. (A) Circa 52 Ma: potential pre-magmatic convergence of the upper plate (nascent Philippine Sea plate) and lower Pacific plate scrapes sediment off Pacific plate ocean crust. (B) circa 51.8 Ma: foundering of the Pacific plate leads to upwelling and decompression melting of Philippine Sea plate mantle to form Forearc basalt (FAB) suite. (C) *circa* 51.5 Ma: amphibolite facies melting of the foundering Pacific plate ocean crust fluxes the mantle residue of FAB decompression melting; further decompression melting of this metasomatized FAB residue forms LSB series of lavas at an axial spreading center. (D) circa 51 Ma: continued decompression melting of FAB residual mantle in response to addition of sediment-derived melt of accumulated off-scraped sediment. See Li et al. (2019) for isotopic constraints and Reagan et al. (2019) for age constraints.

## References:


Adachi, Y., and S. Miyashita, 2003, Geology and petrology of the plutonic complexes in the Wadi Fizh area: Multiple magmatic events and segment structure in the northern Oman ophiolite, Geochem. Geophys. Geosyst., 4(9), 8619, doi:10.1029/ 2001GC000272, 2003.

Almeev, R. R., Holtz, F., Koepke, J., Parat, F., & Botcharnikov, R. E. (2007). The effect of $H_2O$ on olivine crystallization in MORB: Experimental calibration at 200 MPa. *American Mineralogist*, 92(4), 670-674.

Almeev, R. R., Holtz, F., Koepke, J., and Parat, F., 2012, Experimental calibration of the effect of H2O on plagioclase crystallization in basaltic melt at 200 MPa: American Mineralogist, v. 97, no. 7, p. 1234–1240

Ariskin, A.A. (1999), Phase equilibria modeling in igneous petrology: Use of COMAGMAT model for simulating fractionation of ferro-basaltic magmas and the genesis of high-alumina basalt. *Journal of Volcanology and Geothermal Research,* v. 90, p. 115−162. doi.org/10.1016/S0377-0273(99)00022-0

Benn K and Laurent, R, 1987, Intrusive suite documented in the Troodos ophiolite plutonic complex, Cyprus Geology (1987) 15 (9): 821-824. doi.org/10.1130/0091-7613(1987)15<821:ISDITT>2.0.CO;2

Bloomer, S. H. (1983). Distribution and origin of igneous rocks from the landward slopes of the Mariana Trench: Implications for its structure and evolution. *Journal of Geophysical Research: Solid Earth*, *88*(B9), 7411-7428. doi.org/10.1029/JB088iB09p07411.

Bloomer, S.H., Hawkins, J.W. (1987), Petrology and geochemistry of boninite series volcanic rocks from the Mariana trench. *Contributions to Mineralogy and Petrology* 97, 361-377. doi.org/10.1007/BF00371999

Bortolotti, V., Marroni, M., Pandolfi, L., Principi, G. T., & Saccani, E. (2002). Interaction between mid-ocean ridge and subduction magmatism in Albanian ophiolites. *The Journal of Geology*, 110(5), 561-576

Brounce, M., Kelley, K.A., Cottrell, E., Reagan, M.K. (2015), Temporal evolution of mantle wedge oxygen fugacity during subduction initiation. *Geology*, 43, 775-778. doi.org/10.1130/G36742.1

Cameron, W.E., 1985, Petrology and origin of primitive lavas from the Troodos ophiolite, Cyprus. *Contributions to Mineralogy and Petrology* 89, 239-255. doi.org/10.1007/BF00379457

Cameron, W. E., Nisbet, E. G., & Dietrich, V. J. (1979). Boninites, komatiites and ophiolitic basalts. *Nature*, 280(5723), 550-553.

Cameron, W. E. (1985). Petrology and origin of primitive lavas from the Troodos ophiolite, Cyprus. *Contributions to Mineralogy and Petrology*, 89(2-3), 239-255.

Chapp, E., B. Taylor, A. Oakley, and G. F. Moore (2008), A seismic stratigraphic analysis of Mariana forearc basin evolution, Geochemistry Geophysics. Geosystems, 9, Q10X02, doi:10.1029/2008GC001998.

Chapman, T., Clarke, G. L., Daczko, N. R. (2019) The role of buoyancy in the fate of ultra-high-pressure eclogite. Scientific Reports. DOI: 10.1038/s41598-019-56475-y.

Christeson, G. L., S. Morgan, S. Kodaira, M. Yamashita, R. R. Almeev, K. Michibayashi, T. Sakuyama, E. C. Ferre, and W. Kurz (2016), Physical properties and seismic structure of Izu-Bonin-Mariana fore-arc crust: Results from IODP Expedition 352 and comparison with oceanic crust, *Geochemistry, Geophysics, Geosystems*, 17, 4973–4991. doi:10.1002/2016GC006638.

Coulthard, D.A. Jr., Reagan, M.K., Shimizu, K., Bindeman, I.N., Brounce, M., Almeev, R., Ryan, J., Shervais, J., & Pearce, J. (2020). The evolution of nascent magmatism after subduction initiation as recorded in volcanic glasses recovered during IODP Expedition 352. *Geochemistry, Geophysics, Geosystems*. doi:10.1029/2020GC009054.

Crameri, F., Tackley, P.J., Meilick, I., Gerya, T.V., and Kaus, B.J.P. (2012), A free plate surface and weak oceanic crust produce single-sided subduction on Earth. *Geophysical Research Letters*, 39, L03306. doi:10.1029/2011GL050046.

Crawford, A.J., Falloon, T.J., and Green, D.H. (1989), Classification, petrogenesis and tectonic setting of boninites. *In* Crawford, A.J. (Ed.), *Boninites and Related Rocks:* London (Unwin Hyman), 1–49. ISBN-13:9780044450030

DeBari, S.M., Taylor, B., Spencer, K., and Fujioka, K. (1999). A trapped Philippine Sea plate origin for MORB from the inner slope of the Izu-Bonin Trench. *Earth and Planetary Science Letters*, 174(1–2):183-197. doi:10.1016/S0012-821X(99)00252-6

Deschamps, A., and Lallemand, S. (2002), The West Philippine Basin: An Eocene to early Oligocene back arc basin opened between two opposed subduction zones. *Journal of Geophysical Research*, 107, doi:10.1029/2001JB001706

Deschamps, A., & Lallemand, S. (2003). Geodynamic setting of Izu-Bonin-Mariana boninites. *Geological Society, London, Special Publications*, *219*(1), 163-185

Dobson, P.F., and O'Neil, J.R., 1987, Stable isotope compositions and water contents of boninite series volcanic rocks from Chichi-jima, Bonin Islands, Japan: Earth and Planetary Science Letters, v. 82, p. 75–86, https:// doi .org /10 .1016 /0012 -821X (87)90108 -7.

Dobson, P.F., Blank, J.G., Maruyama, S., Liou (2006), Petrology and geochemistry of boninite-series rocks, Chichijima, Bonin Islands, Japan. *International Geology Review* 48(8), 669-701. doi: 10.2747/0020-6814.48.8.669

Faccenna, C., Di Giuseppe, E., Funiciello, F., Lallemand, S., & Van Hunen, J. (2009). Control of seafloor aging on the migration of the Izu–Bonin–Mariana trench. *Earth and Planetary Science Letters*, 288(3-4), 386-398.

Faccenna, C., Holt, A. F., Becker, T. W., Lallemand, S., & Royden, L. H. (2018). Dynamics of the Ryukyu/Izu-

Bonin-Marianas double subduction system. *Tectonophysics*, 746, 229-238.

Falloon, T.J., and Danyushevsky, L.V., 2000, Melting of refractory mantle at 1.5, 2.0 and 2.5 GPa under anhydrous and H2O-undersaturated conditions: Implications for the petrogenesis of high-Ca boninites and the influence of subduction components on mantle melting: *Journal of Petrology*, 41, 257–283, https:// doi .org /10.1093 /petrology/41.2.257.

Falloon, T.J., Danyushevsky, L.V., Crawford, A.J., Meffre, S., Woodhead, J.D., and Bloomer, S.H., 2008, Boninites and adakites from the northern termination of the Tonga Trench: Implications for adakite petrogenesis: Journal of Petrology, v. 49, p. 697–715, https:// doi .org /10 .1093 /petrology /egm080.

Fryer, P. (1995), Geology of the Mariana Trough. *in* Taylor B., ed., *Backarc basins; tectonics and magmatism*, Springer, New York, 237-279. doi.org/10.1007/978-1-4615-1843-3_6.

Gong, W., Xing, J., & Jiang, X. (2018). Heterogeneous subduction structure within the Pacific plate beneath the Izu-Bonin arc. *Journal of Geodynamics*, 116, 1-12.

Gurnis, M., Hall, C. and Lavier, L. (2004), Evolving force balance during incipient subduction. *Geochemistry, Geophysics, Geosystems*, 5, Q07001. doi.org/10.1029/2003GC000681

Hall, C.E., Gurnis, M., Sdrolias, M., Lavier, L.L., and Dietmar Müller, R.(2003), Catastrophic initiation of subduction following forced convergence across fracture zones. *Earth and Planetary Science Letters*, 212(1–2):15–30. http://dx.doi.org/10.1016/S0012-821X(03)00242-5

Hickey, R. L., & Frey, F. A. (1982). Geochemical characteristics of boninite series volcanics: implications for their source. *Geochimica et Cosmochimica Acta*, *46*(11), 2099-2115.

Hickey-Vargas, R., Yogodzinski, G.M., Ishizuka, O., McCarthy, A., Bizimis, M., Kusano, Y., Savov, I.P., Arculus, R., (2018), Origin of depleted basalts during subduction initiation and early development of the Izu-Bonin-Mariana Island arc: Evidence from IODP Expedition 351 Site U1438, Amami-Sankaku Basin. *Geochimica et Cosmochimica Acta*, 229, 85-111. doi:10.1016/j.gca.2018.03.007

Hoeck, V., Koller, F., Meisel, T., Onuzi, K., & Kneringer, E. (2002). The Jurassic South Albanian ophiolites: MOR-vs. SSZ-type ophiolites. *Lithos*, 65(1-2), 143-164.

Ishikawa, T., Nagaishi, K., & Umino, S. (2002). Boninitic volcanism in the Oman ophiolite: Implications for thermal condition during transition from spreading ridge to arc. Geology, 30(10), 899-902. doi.org/10.1130/0091-7613(2002)030<0899:BVITOO>2.0.CO;2

Ishizuka, O., Hickey-Vargas, R., Arculus, R.J., Yogodzinski, G.M., Savov, I.P., Kusano, Y., McCarthy, A., Brandl, P.A., Sudo, M. (2018), Age of Izu–Bonin–Mariana arc basement. *Earth and Planetary Science Letters*, 481, 80-90. doi:10.1016/j.epsl.2017.10.023

Ishizuka, O., Kimura, J.-I., Li, Y.B., Stern, R.J., Reagan, M.K., Taylor, R.N., Ohara, Y., Bloomer, S.H., Ishii, T., Hargrove, U.S., III, and Haraguchi, S., 2006, Early stages in the evolution of Izu-Bonin arc volcanism: new age, chemical, and isotopic constraints. *Earth and Planetary Science Letters*, 250(1–2):385–401. doi:10.1016/j.epsl.2006.08.007.

Ishizuka, O., Tani, K., Reagan, M.K., Kanayama, K., Umino, S., Harigane, Y., Sakamoto, I., Miyajima, Y., Yuasa, M., and Dunkley, D.J. (2011a), The timescales of subduction initiation and subsequent evolution of an oceanic island arc. *Earth and Planetary Science Letters*, 306(3-4), 229-240. doi:10.1016/j.epsl.2011.04.006

Ishizuka, O., Taylor, R.N., Yuasa, M., and Ohara,Y. (2011b), Making and breaking an island arc: A new perspective from the Oligocene Kyushu-Palau arc, Philippine Sea: *Geochemistry, Geophysics, Geosystems*, 12, Q05005. doi:10.1029/2010GC003440.

Ishizuka, O., Taylor, R.N., Ohara, Y., Yuasa, M. (2013), Upwelling, rifting, and age-progressive magmatism from the Oki-Daito mantle plume. *Geology*, 41 (9): 1011–1014. doi:10.1130/G34525.1

Ishizuka, O and Taylor, RN and Umino, S and Kanayama, K, 2020, Geochemical evolution of arc and slab following subduction initiation: a record from the Bonin Islands, Japan, Journal of Petrology}, doi: 10.1093/petrology/egaa050.

Jaxybulatov, K., Koulakov, I., & Dobretsov, N. L. (2013). Segmentation of the Izu-Bonin and Mariana slabs based on the analysis of the Benioff seismicity distribution and regional tomography results. *Solid Earth*, 4(1).

Jenner, F.E., & O'Neill, H.S.C. (2012). Analysis of 60 elements in 616 ocean floor basaltic glasses. Geochemistry, Geophysics, Geosystems, 13(2). doi: 10.1029/2011GC004009

Kelley, KA, Plank, T, Ludden, J. and Staudigel, H, 2003, Composition of altered oceanic crust at ODP Sites 801 and 1149, Geochemistry, Geophysics, Geosystems, 4(6), 8910, doi:10.1029/2002GC000435.

Kong, X., Li, S., Wang, Y., Suo, Y., Dai, L., Geli, L., ... & Wang, P. (2018). Causes of earthquake spatial distribution beneath the Izu-Bonin-Mariana Arc. *Journal of Asian Earth Sciences*, 151, 90-100.

Kurz, W., Micheuz, P, Christeson, GL, Reagan, M, Shervais, JW, Kutterolf, S, Robertson, AHF, Krenn, K, Michibayashi, K, Quandt, D. (2019) Tectonic evolution of the outer Izu-Bonin forearc: implications for a 15 Ma hiatus between Pacific Plate subduction initiation and forearc extension. *Geochemistry, Geophysics, Geosystems*. DOI:10.1029/2019GC008329.

Kuroda, N., Shiraki K. (1975). Boninite and related rocks of Chichijima, Bonin Islands, Japan., Rep. Faculty Sci., Shizuoka University, 10, 145-155.

Kutterolf, S., Schindlbeck, J. C., Robertson, A. H. F., Avery, A., Baxter, A. T., Petronotis, K., and Wang, K.-L. (2018), Tephrostratigraphy and provenance from IODP Expedition 352, Izu-Bonin arc: Tracing tephra sources and volumes from the Oligocene to recent. *Geochemistry, Geophysics, Geosystems*, 19, 150–174. doi:10.1002/2017GC007100

Le Bas, M. J. (2000). IUGS reclassification of the high-Mg and picritic volcanic rocks. *Journal of Petrology*, 41(10), 1467-1470.

Lee C. A., Luffi P., Plank T., Dalton H. and Leeman W.P. (2009), Constraints on the depths and temperatures of basaltic magma generation on earth and other terrestrial planets using new thermobarometers for mafic magmas. *Earth and Planetary Science Letters*, 279, 20-33. doi:10.1016/j.epsl.2008.12.020.

Leng, W., Gurnis M., and Asimow, P. (2012), From basalts to boninites: The geodynamics of volcanic expression during induced subduction initiation. *Lithosphere*, 4/6, 511–523. doi:10.1130/L215.1

Li, H-Y, Taylor, R, Julie Prytulak, Shervais, JW, Ryan, JG, Godard, M, Reagan, MK, Pearce, JA, 2019, Radiogenic isotopes document the start of subduction in the western Pacific. *Earth and Planetary Science Letters*. https://doi.org/10.1016/j.epsl.2019.04.041

MacLeod, C.J., Lissenberg, C.J., Bibby, L.E. (2013), "Moist MORB" axial magmatism in the Oman ophiolite: The evidence against a mid-ocean ridge origin. *Geology*, 41/4, 459–462. doi:/10.1130/G33904.1.

Maunder, B., Prytulak, J., Goes, S., & Reagan, M. (2020). Rapid subduction initiation and magmatism in the Western Pacific driven by internal vertical forces. Nature Communications. https://doi.org/10.1038/s41467-020-15737-4

Meade, B.J. (2007), Present-day kinematics at the India-Asia collision zone. *Geology*, 35(1) 81-84, doi.org/10.1130/G22924A.1

Meijer, A. (1980). Primitive arc volcanism and a boninite series: examples from western Pacific island arcs, in DE Hayes (ed) Tectonic and Geologic Evolution of South-east Asian Seas and Islands, Geophys. Monogr. Ser., vol. 23, 269-282, AGU, Washington, D. C., DOI: 10.1029/GM023p0269

Meijer, A., Anthony, A., Reagan, M. (1981). Petrology of volcanic rocks from the fore-arc sites. *In* Hussong, D. M., Uyeda, S., et al., *Init. Repts. DSDP*, 60: Washington (U.S. Govt. Printing Office), 709-729.

doi:10.2973/dsdp.proc.60.138.1982.

Metcalf RV, Shervais J.W. (2008), Supra-Subduction Zone (SSZ) Ophiolites: Is There Really an "Ophiolite Conundrum"? In: Wright JE, Shervais JW (eds) Ophiolites, Arcs, and Batholiths: A Tribute to Cliff Hopson. *Geological Society of America, Special Paper* 438, 191-222. doi:10.1130/2008.2438(07).

Mitchell, A. L., & Grove, T. L. (2015). Melting the hydrous, subarc mantle: the origin of primitive andesites. *Contributions to Mineralogy and Petrology*, 170(2), 13.

Miyashiro, A. (1973). The Troodos ophiolitic complex was probably formed in an island arc. *Earth and Planetary Science Letters*, 19(2), 218-224.

Morishita, T., Tani, K., Shukuno, H., Harigane, Y., Tamura, A., Kumagai, H., & Hellebrand, E. (2011). Diversity of melt conduits in the Izu-Bonin-Mariana forearc mantle: Implications for the earliest stage of arc magmatism. *Geology*, 39(4), 411-414. doi.org/10.1130/G31706.1.

Mrozowski, C.L. Hayes, D.E. (1979), The evolution of the Parece Vela basin, Eastern Philippine sea. *Earth and Planetary Science Letters*, 46, 49–67. 10.1016/0012-821X(79)90065-7.

Najman, Y., Appel, E., Boudagher-Fadel, M., Bown, P., Carter, A., Garzanti, E., Godin, L., Han, J., Liebke, U., Oliver, G., Parrish, R., Vezzoli. G. (2010), Timing of India-Asia collision: Geological, biostratigraphic, and palaeomagnetic constraints. *Journal of Geophysical Research*, 115, B12416, doi:10.1029/2010JB007673.

Niu, Y, 1997, Mantle Melting and Melt Extraction Processes beneath Ocean Ridges: Evidence from Abyssal Peridotites, Journal of Petrology, 38/8, 1047–1074, https://doi.org/10.1093/petroj/38.8.1047.

Okino, K., Kasuga, S., Ohara, Y. (1998), A new scenario of the Parece Vela basin genesis. *Marine Geophysical Researches*, 20 (1) (1998), pp. 21–40. doi:10.1023/A:1004377422118.

Parkinson, I.J. and Pearce, J.A. (1998). Peridotites from the Izu–Bonin–Mariana forearc (ODP Leg 125): evidence for mantle melting and melt–mantle interaction in a supra-subduction zone setting. *Journal of Petrology*, *39*(9), pp.1577-1618. doi.org/10.1093/petroj/39.9.1577.

Patino, L. C., Velbel, M. A., Price, J. R., & Wade, J. A. (2003). Trace element mobility during spheroidal weathering of basalts and andesites in Hawaii and Guatemala. *Chemical Geology*, 202(3-4), 343-364

Patriat, M, Falloon, T, Danyushevsky, L, Collot, J, Jean, MM, Hoernle, K, Hauff, F, Maas, R, Woodhead, JD, Feig, ST, 2019, Subduction initiation terranes exposed at the front of a 2 Ma volcanically-active subduction zone. Earth and Planetary Science Letters, 508, 30-40. doi.org/10.1016/j.epsl.2018.12.011

Pearce, J.A., and Reagan, M.K. (2019). Identification classification and interpretation of boninites from the Recent-Eoarchean geologic record using Si-Mg-Ti systematics. Geosphere, 15, 1–30, https://doi.org/10.1130/GES01661.1.

Pearce, J.A. and Robinson, P.T. (2010), The Troodos ophiolitic complex probably formed in a subduction initiation, slab edge setting. *Gondwana Research*, 18(1):60–81. doi:10.1016/j.gr.2009.12.003

Pearce, J.A., Lippard, S.J., and Roberts, S. (1984), Characteristics and tectonic significance of supra-subduction zone ophiolites. *In* Kokelaar, B.P., and Howells, M.F. (Eds.), *Marginal Basin Geology: Volcanic and Associated Sedimentary and Tectonic Processes in Modern and Ancient Arginal Basins.* Geological Society Special Publication, 16(1):74–94. doi:10.1144/GSL.SP.1984.016.01.06

Pearce, J. A., Lann, S. R., Arculus, R. J., Murton, B. J., Ishii, T., Peate, D. W. & Parkinson, I. J. (1992), Boninite and harzburgite from Leg 125 (Bonin-Mariana fore-arc): A case study of magma genesis during the initial stages of subduction. *In*: Fryer, P., Peace, J. A. & Stokking, L. B. (eds) *Proceedings of the Ocean Drilling Program, Scientific Results*, 125. College Station, TX: Ocean Drilling Program, 623-659. 10.2973/odp.proc.sr.125.172.1992.

Perrin, A., Goes, S., Prytulak, J., Davies, DR, Wilson, C, Kramer, S (2016), Reconciling mantle wedge thermal

structure with arc lava thermobarometric determinations in oceanic subduction zones. *Geochemistry, Geophysics, Geosystems*, 17, 4105-4127, doi.org/10.1002/2016GC006527

Petersen, J., 1891, Der boninit von Peel Island: Jahrbuch Hamburgischen Wissenschaftlichen Anstalten, v. 8, p. 341–349.

Plank, T., & Langmuir, C. H. (1998). The chemical composition of subducting sediment and its consequences for the crust and mantle. *Chemical geology*, 145(3-4), 325-394

Python, M., & Ceuleneer, G. (2003). Nature and distribution of dykes and related melt migration structures in the mantle section of the Oman ophiolite. *Geochemistry, Geophysics, Geosystems*, 4(7).

Reagan, M.K., Ishizuka, O., Stern, R.J., Kelley, K.A., Ohara, Y., Blichert-Toft, J., Bloomer, S.H., Cash, J., Fryer, P., Hanan, B.B., Hickey-Vargas, R., Ishii, T., Kimura, J.-I., Peate, D.W., Rowe, M.C., and Woods, M. (2010), Fore-arc basalts and subduction initiation in the Izu-Bonin-Mariana system. *Geochemistry, Geophysics, Geosystems*, 11(3):Q03X12. doi.:10.1029/2009GC002871

Reagan, M.K., McClelland, W.C., Girard, G., Goff, K.R., Peate, D.W., Ohara, Y., Stern, R.J. (2013), The geology of the southern Mariana fore-arc crust: implications for the scale of Eocene volcanism in the western Pacific. *Earth and Planetary Science Letters*, 380:41-1. doi:10.1016/j.epsl.2013.08.013

Reagan, M.K., Pearce, J.A., Petronotis, K., Almeev, R., Avery, A.A., Carvallo, C., Chapman, T., Christeson, G.L., Ferré, E.C., Godard, M., Heaton, D.E., Kirchenbaur, M., Kurz, W., Kutterolf, S., Li, H.Y., Li, Y., Michibayashi, K., Morgan, S., Nelson, W.R., Prytulak, J., Python, M., Robertson, A.H.F., Ryan, J.G., Sager, W.W., Sakuyama, T., Shervais, J.W., Shimizu, K., and Whattam, S.A., (2015a), Expedition 352 summary. *In* Reagan, M.K., Pearce, J.A., Petronotis, K., and the Expedition 352 Scientists, *Izu-Bonin-Mariana Fore Arc*. Proceedings of the International Ocean Discovery Program, 352: College Station, TX (International Ocean Discovery Program). doi:10.14379/iodp.proc.352.101.2015

Reagan, M.K., Pearce, J.A., Petronotis, K., Almeev, R., Avery, A.A., Carvallo, C., Chapman, T., Christeson, G.L., Ferré, E.C., Godard, M., Heaton, D.E., Kirchenbaur, M., Kurz, W., Kutterolf, S., Li, H.Y., Li, Y., Michibayashi, K., Morgan, S., Nelson, W.R., Prytulak, J., Python, M., Robertson, A.H.F., Ryan, J.G., Sager, W.W., Sakuyama, T., Shervais, J.W., Shimizu, K., and Whattam, S.A., (2015b), Site U1440. *In* Reagan, M.K., Pearce, J.A., Petronotis, K., and the Expedition 352 Scientists, *Izu-Bonin-Mariana Fore Arc*. Proceedings of the International Ocean Discovery Program, 352: College Station, TX (International Ocean Discovery Program). http://dx.doi.org/10.14379/iodp.proc.352.104.2015.

Reagan, M.K., Pearce, J.A., Petronotis, K., Almeev, R., Avery, A.A., Carvallo, C., Chapman, T., Christeson, G.L., Ferré, E.C., Godard, M., Heaton, D.E., Kirchenbaur, M., Kurz, W., Kutterolf, S., Li, H.Y., Li, Y., Michibayashi, K., Morgan, S., Nelson, W.R., Prytulak, J., Python, M., Robertson, A.H.F., Ryan, J.G., Sager, W.W., Sakuyama, T., Shervais, J.W., Shimizu, K., and Whattam, S.A., (2015c), Site U1441. *In* Reagan, M.K., Pearce, J.A., Petronotis, K., and the Expedition 352 Scientists, *Izu-Bonin-Mariana Fore Arc*. Proceedings of the International Ocean Discovery Program, 352: College Station, TX (International Ocean Discovery Program). http://dx.doi.org/10.14379/iodp.proc.352.105.2015.

Reagan, M.K., Pearce, J.A., Petronotis, K., Almeev, R., Avery, A.A., Carvallo, C., Chapman, T., Christeson, G.L., Ferré, E.C., Godard, M., Heaton, D.E., Kirchenbaur, M., Kurz, W., Kutterolf, S., Li, H.Y., Li, Y., Michibayashi, K., Morgan, S., Nelson, W.R., Prytulak, J., Python, M., Robertson, A.H.F., Ryan, J.G., Sager, W.W., Sakuyama, T., Shervais, J.W., Shimizu, K., and Whattam, S.A., (2015d), Site U1439. *In* Reagan, M.K., Pearce, J.A., Petronotis, K., and the Expedition 352 Scientists, *Izu-Bonin-Mariana Fore Arc*. Proceedings of the International Ocean Discovery Program, 352: College Station, TX (International Ocean Discovery Program). http://dx.doi.org/10.14379/iodp.proc.352.103.2015.

Reagan, M.K., Pearce, J.A., Petronotis, K., Almeev, R., Avery, A.A., Carvallo, C., Chapman, T., Christeson, G.L.,

Ferré, E.C., Godard, M., Heaton, D.E., Kirchenbaur, M., Kurz, W., Kutterolf, S., Li, H.Y., Li, Y., Michibayashi, K., Morgan, S., Nelson, W.R., Prytulak, J., Python, M., Robertson, A.H.F., Ryan, J.G., Sager, W.W., Sakuyama, T., Shervais, J.W., Shimizu, K., and Whattam, S.A., (2015e), Site U1442. *In* Reagan, M.K., Pearce, J.A., Petronotis, K., and the Expedition 352 Scientists, *Izu-Bonin-Mariana Fore Arc*. Proceedings of the International Ocean Discovery Program, 352: College Station, TX (International Ocean Discovery Program). http://dx.doi.org/10.14379/iodp.proc.352.106.2015.

Reagan, M.K., Pearce, J.A., Petronotis, K., Almeev, R., Avery, A.A., Carvallo, C., Chapman, T., Christeson, G.L., Ferré, E.C., Godard, M., Heaton, D.E., Kirchenbaur, M., Kurz, W., Kutterolf, S., Li, H.Y., Li, Y., Michibayashi, K., Morgan, S., Nelson, W.R., Prytulak, J., Python, M., Robertson, A.H.F., Ryan, J.G., Sager, W.W., Sakuyama, T., Shervais, J.W., Shimizu, K., and Whattam, S.A., (2015e), Expedition 352 Methods. *In* Reagan, M.K., Pearce, J.A., Petronotis, K., and the Expedition 352 Scientists, *Izu-Bonin-Mariana Fore Arc*. Proceedings of the International Ocean Discovery Program, 352: College Station, TX (International Ocean Discovery Program). fhttp://dx.doi.org/10.14379/iodp.proc.352.102.2015.

Reagan, M.K., Pearce, J.A., Petronotis, K., Almeev, R.R., Avery A.J., Carvallo, C., Chapman, T., Christeson, G.L., Ferré, E.C., Godard, M., Heaton, D.E., Kirchenbaur, M., Kurz, W., Kutterolf, S., Li, H., Li, Y., Michibayashi, K., Morgan, S., Nelson, W.R., Prytulak, J., Python, M., Robertson, A.H.F., Ryan, J.G., Sager, W.W., Sakuyama, T., Shervais, J.W., Shimizu, K., and Whattam, S.A., (2017), Subduction initiation and ophiolite crust: new insights from IODP drilling: *International Geology Review*, 59, 1-12. doi:10.1080/00206814.2016.1276482.

Reagan, MK, Heaton, DE, Schmitz, MD, Pearce, JA, Shervais, JW, and Koppers, AAP, 2019, Forearc ages reveal extensive short-lived and rapid seafloor spreading following subduction initiation. *Earth and Planetary Science Letters*, 506, 520–529, doi.org/10.1016/j.epsl.2018.11.020.

Ribeiro, J.M., Stern, R.J., Kelley, K.A., Shaw, A.M., Martinez, F., and Ohara, Y., 2015, Composition of the slab-derived fluids released beneath the Mariana forearc: Evidence for shallow dehydration of the subducting plate: Earth and Planetary Science Letters, v. 418, p. 136–148, https:// doi .org /10 .1016 /j .epsl .2015 .02 .018.

Ribeiro, J.M., Stern, R.J., Martinez, F., Ishizuka, O., Merle, S.G., Kelley, K.A., Anthony, E.Y., Ren, M., Ohara, Y., Reagan, M., Girard, G., and Bloomer, S.H., 2013, Geodynamic evolution of a forearc rift in the southernmost Mariana arc: The Island Arc, v. 2, no. 4, p. 453–476, https:// doi .org /10 .1111 /iar .12039.

Robertson, A. H. F., Kutterolf, S., Avery, A. J., Baxter, A. T., Petronotis, K., Acton, G. D., Carvallo, C. and Schindlbeck, J. C. (2017), Depositional setting, provenance and tectonic-volcanic setting of Eocene-Recent deep-sea sediments of the oceanic Izu-Bonin forearc, NW Pacific (IODP Expedition 352). *International Geology Review*, 1–39. doi:10.1080/00206814.2017.1393634

Rollinson, H.R. (1995). Using geochemical data: evaluation, presentation, interpretation. Routledge, Oxon, UK, ISBN 13: 978-0-582-06701-1, 467 pp.

Ryan, J.G., J.W. Shervais, Y. Li, M.K. Reagan, H. Li, D. Heaton, M. Godard, M. Kirchenbaur, S. Whattam, J.A. Pearce, T. Chapman, W. Nelson, J. Prytulak, K. Shimizu, K. Petronotis, and the IODP Expedition 352 Scientific Team (2017), Application of a handheld X-ray fluorescence spectrometer for real-time, high-density quantitative analysis of drilled igneous rocks and sediments during IODP Expedition 352. *Chemical Geology*, 451, 55–66. doi: 10.1016/j.chemgeo.2017.01.007

Salters, V.J.M., Stracke, A., 2004, Composition of the depleted mantle, *Geochemistry, Geophysics, Geosystems*, 5, Q05004, doi:10.1029/2003GC000597.

Savov, I. P., Hickey-Vargas, R., D'Antonio, M., Ryan, J. G. and Spadea, P. (2006a), Petrology and geochemistry of West Philippine Basin basalts and early Palau–Kyushu arc volcanic clasts from ODP Leg 195, Site 1201D: Implications for the early history of the Izu–Bonin–Mariana arc. *Journal of Petrology* 47, 277–299.

10.1093/petrology/egi075.

Savov, I. P., Shirey, S. B., Horan, M. F., Mock, T. D. (2006b). Ancient mantle trapped in the Mariana arc-basin system: Insights from the platinum group elements and Os isotopes. American Geophysical Union, Fall Meeting 2006, abstract V51F-05.

Senda, R, Shimizu, K., Suzuki, K., (2016) Ancient depleted mantle as a source of boninites in the Izu-Bonin-Mariana arc: Evidence from Os isotopes in Cr-spinel and magnetite Chemical Geology, (2016), 439. 10.1016/j.chemgeo.2016.06.018.

Shaw, D. M. (1970). Trace element fractionation during anatexis. Geochimica et Cosmochimica Acta, 34(2), 237-243.

Shervais, J.W. (1982) Ti-V plots and the petrogenesis of modern and ophiolitic lavas: Earth and Planetary Science Letters, v. 59, p. 101–118, https:// doi .org /10 .1016 /0012 -821X (82)90120 -0.

Shervais, J.W., (1990) Island arc and ocean crust ophiolites: contrasts in the petrology, geochemistry, and tectonic style of ophiolite assemblages in the California coast ranges. Ophiolites: Oceanic Crustal Analogues, J.C. Malpas, E.M. Moores, A. Panayiotou, and C. Xenophontos (eds.), The Geological Survey Department, Nicosia, Cyprus, 507-520.

Shervais, J.W. (2001), Birth, Death, and Resurrection: The Life Cycle of Suprasubduction Zone Ophiolites, *Geochemistry, Geophysics, Geosystems*, vol. 2, (Paper number 2000GC000080), 20,925 words, 8 figures, 3 tables. doi:0.1029/2000GC000080.

Shervais, J.W. (2008) Tonalites, Trondhjemites, and Diorites of the Elder Creek Ophiolite, California: Low Pressure Slab Melting and Reaction with the Mantle Wedge, in James E. Wright and John W. Shervais, editors, Ophiolites, Arcs, and Batholiths: A Tribute to Cliff Hopson: Geological Society of America Special Paper 438, p. 113–132, doi:10.1130/2008.2438(03).

Shervais, JW and Jean, MM (2012) Inside the Subduction Factory: Fluid mobile trace elements in the mantle wedge above a subduction zone, *Geochimica et Cosmochimica Acta*, 95, 270-285. doi:10.1016/j.gca.2012.07.006

Shervais, J.W. and Johnson, K.T. (2019) September. Subduction Initiation Peridotites of the Western Pacific and Implications for Boninite Genesis: Results from IODP Expedition 366. In GSA Annual Meeting in Phoenix, Arizona, USA-2019. GSA.

Shervais, J.W., Murchey, B., Kimbrough, D.L., Renne, P., and Hanan, B.B. (2005) Radioisotopic and Biostratigraphic Age Relations in the Coast Range Ophiolite, Northern California: Implications for the Tectonic Evolution of the Western Cordillera, Geological Society of America Bulletin, v. 117, no 5/6, p.633-653.

Shervais, JW, Reagan, MK, Haugen, E, Almeev, R, Pearce, JA, Prytulak, J, Ryan, JG, Whattam, SA, Godard, M, Chapman, T, Li, H-Y, Kurz, W, Nelson, WR, Heaton, DE, Kirchenbaur, M, Shimizu, K, Sakuyama, T, Li, Y, and Vetter, SK (2019) Magmatic Response to Subduction Initiation, Part I: Fore-arc basalts of the Izu-Bonin Arc from IODP Expedition 352. *Geochemistry, Geophysics, Geosystems*, 20/1, 314-338, Article GGGE21778, DOI:10.1029/2018GC007731.

Shervais, JW, Reagan, M, Godard, M, Prytulak, J, Ryan, JG, Pearce, JA, Almeev, R, Li, H, Haugen, E, Chapman, T, Kurz, W, Nelson, WR, Heaton, D, Kirchenbaur, M, Shimizu, K, Sakuyama, T, Vetter, SK, Li, Y, Whattam, SA (2020): Geochemical analyses from the Boninite suite lavas and the Izu-Bonin forearc from IODP Hole 352-U1439A and 352-U1442A. PANGAEA, https://doi.pangaea.de/10.1594/PANGAEA.921304.

Sobolev, A.V., and Danyushevsky, L.V. (1994) Petrology and geochemistry of boninites from the north termination of the Tonga Trench: Constraints on the generation conditions of primary high-Ca boninite magmas: Journal of Petrology, v. 35, p. 1183–1211, doi:10.1093 /petrology/35.5.1183.

Sobolev, A.V., Portnyagin, M.V., Dmitriev, L.V., Tsameryan, O.P., Danyushevsky, L.V., Kononkova, N.N.,

Schimizu, N., and Robinson, P.T. (1993) Petrology of ultramafic lavas and associated rocks of the Troodos Massif, Cyprus: Petrology, v. 1, p. 331–361.

Stern, R.J. and Bloomer, S.H. (1992), Subduction zone infancy: examples from the Eocene Izu-Bonin-Mariana and Jurassic California arcs. *Geological Society of America Bulletin*, 104(12):1621–1636. doi:10.1130/0016-7606(1992)104<1621:SZIEFT>2.3. CO;2

Stern, R.J., Fouch, M.J., and Klemperer, S. (2003), An overview of the Izu- Bonin-Mariana subduction factory. *In* Eiler, J. (Ed.), *Inside the Subduction Factory. Geophysical Monograph*, 138:175–222. doi:10.1029/138GM10

Sun, S-S and McDonough, WF, 1989, Chemical and isotopic systematics of oceanic basalts: implications for mantle composition and processes. Geological Society, London, Special Publication 42, 313-345, doi.org/10.1144/GSL.SP.1989.042.01.19

Tamura, A., & Arai, S. (2006). Harzburgite–dunite–orthopyroxenite suite as a record of supra-subduction zone setting for the Oman ophiolite mantle. *Lithos*, 90(1-2), 43-56

Umino, S, and Kushiro, I., 1989, Experimental studies on boninite petrogenesis, in Crawford, A.J., ed., *Boninite and related rocks*: London, Unwin Hyman, p. 89–111.

Umino, S, 1986, Magma mixing in boninite sequence of Chichijima, Bonin Islands. *Journal of Volcanology and Geothermal Research*, 29, 125-157. doi:10.1016/0377-0273(86)90042-9

Umino, S., Kitamura, K., Kanayama, K., Tamura, A., Sakamoto, N., Ishizuka, O., & Arai, S. (2015). Thermal and chemical evolution of the subarc mantle revealed by spinel-hosted melt inclusions in boninite from the Ogasawara (Bonin) Archipelago, Japan. Geology, 43(2), 151-154.

Van der Laan, SR, Flower, MJF, and Koster van Groos, AF, 1989, Experimental evidence for the origin of boninites: near-liquidus phase relations to 7.5 kbar, *In* Crawford, A.J. (Ed.), *Boninites and Related Rocks*: London (Unwin Hyman), 112-147. ISBN-13:9780044450030

Walker, DA and Cameron, WE, 1983, Boninite primary magmas: Evidence from the Cape Vogel Peninsula, PNG. Contributions to Mineraleralogy and Petrology 83: 150. https://doi.org/10.1007/BF00373088.

Whattam, SA, Shervais, JW, Reagan, MK, Pearce, JA, Jones, P, Seo, J, Putirka, K, Chapman, T, Heaton, D, Li, H-Y, Nelson, WR, Shimizu, K, Stern, RJ, 2020, Chemical composition and thermobarometry of IODP Expedition 352 Bonin forearc basalt and boninite minerals: Implications for forearc and ophiolite formation. *American Mineralogist*. https://doi.org/10.2138/am-2020-6640.

Woelki, D., Regelous, M., Haase, KM. Romer, RHW, Beier, C., 2018, Petrogenesis of boninitic lavas from the Troodos Ophiolite, and comparison with Izu–Bonin–Mariana fore-arc crust. Earth and Planetary Science Letters, 498, 203-214, https://doi.org/10.1016/j.epsl.2018.06.041.

Woelki, D., Regelous, M., Haase, KM., Beier, C., 2019, Geochemical mapping of a paleo-subduction zone beneath the Troodos Ophiolite, Chemical Geology, 523, 1-8, https://doi.org/10.1016/j.chemgeo.2019.05.041

Woelki, D., Michael, P., Regelous, M., Haase, KM., 2020, Enrichment of H2O and fluid-soluble trace elements in the Troodos Ophiolite: Evidence for a near-trench origin. Lithos, v356–357, 105299, https://doi.org/10.1016/j.lithos.2019.105299.

Workman, RK and Hart, SR, 2005, Major and trace element composition of the depleted MORB mantle (DMM), Earth and Planetary Science Letters, 231/1–2, 53-72, doi.org/10.1016/j.epsl.2004.12.005.

Wu, J., Suppe, J., Lu, R.-Q., Kanda, R.V.S. (2016), Philippine Sea and East Asian plate tectonics since 52 Ma constrained by new subducted slab reconstruction methods. *Journal of Geophysical Reseasrch Solid Earth*, 121, 4670–4741. doi:10.1002/2016JB012923

Yogodzinski, G.M., Bizimis, M., Hickey-Vargas, R., McCarthy, A., Hocking, B.D., Savov, I.P., Ishizuka, O., Arculus, R. (2018), Implications of eocene-age Philippine sea and forearc basalts for initiation and early

history of the Izu-Bonin-Mariana arc. *Geochimica et Cosmochimica Acta*, 228, 136-156. doi:10.1016/j.gca.2018.02.047.

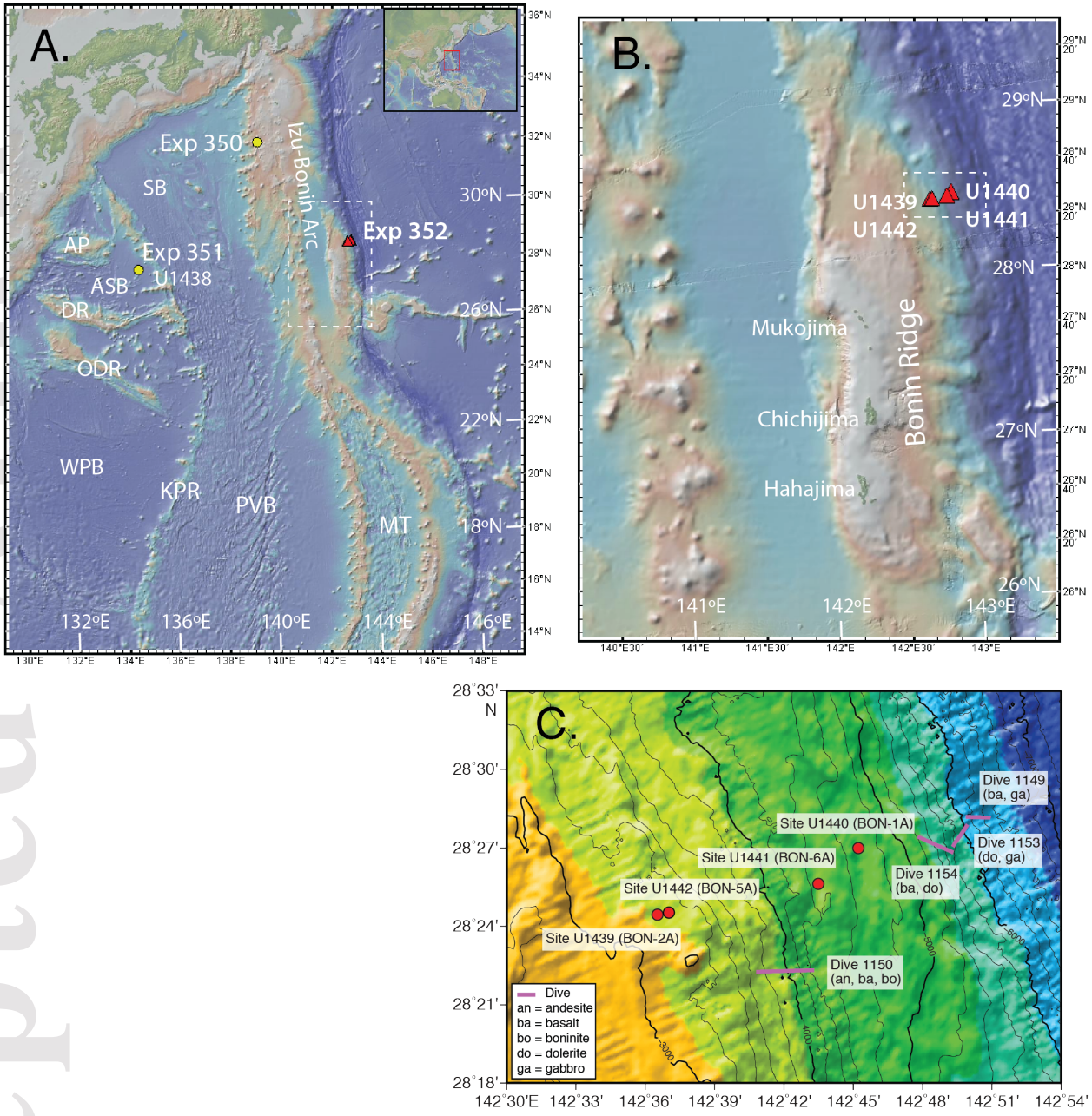

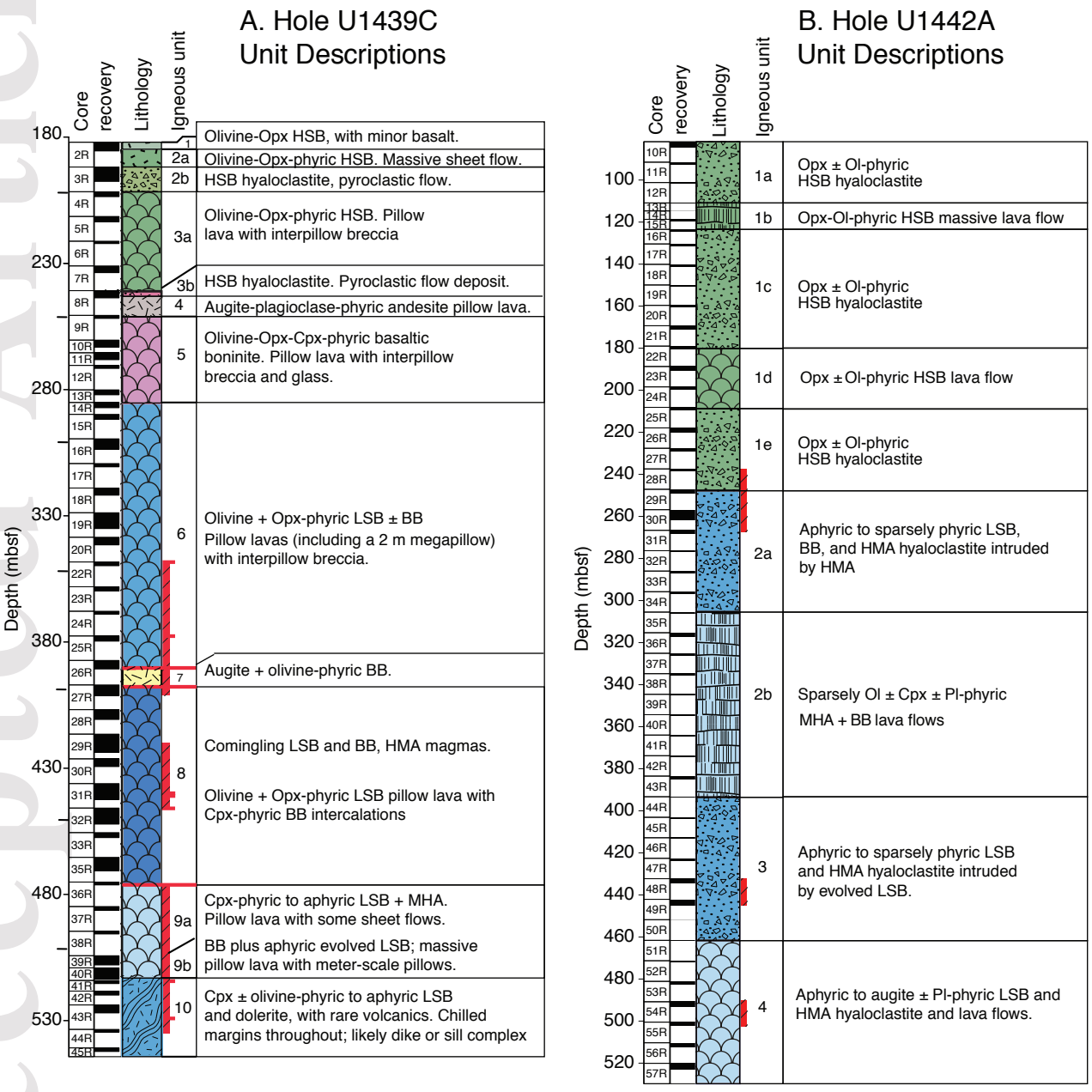

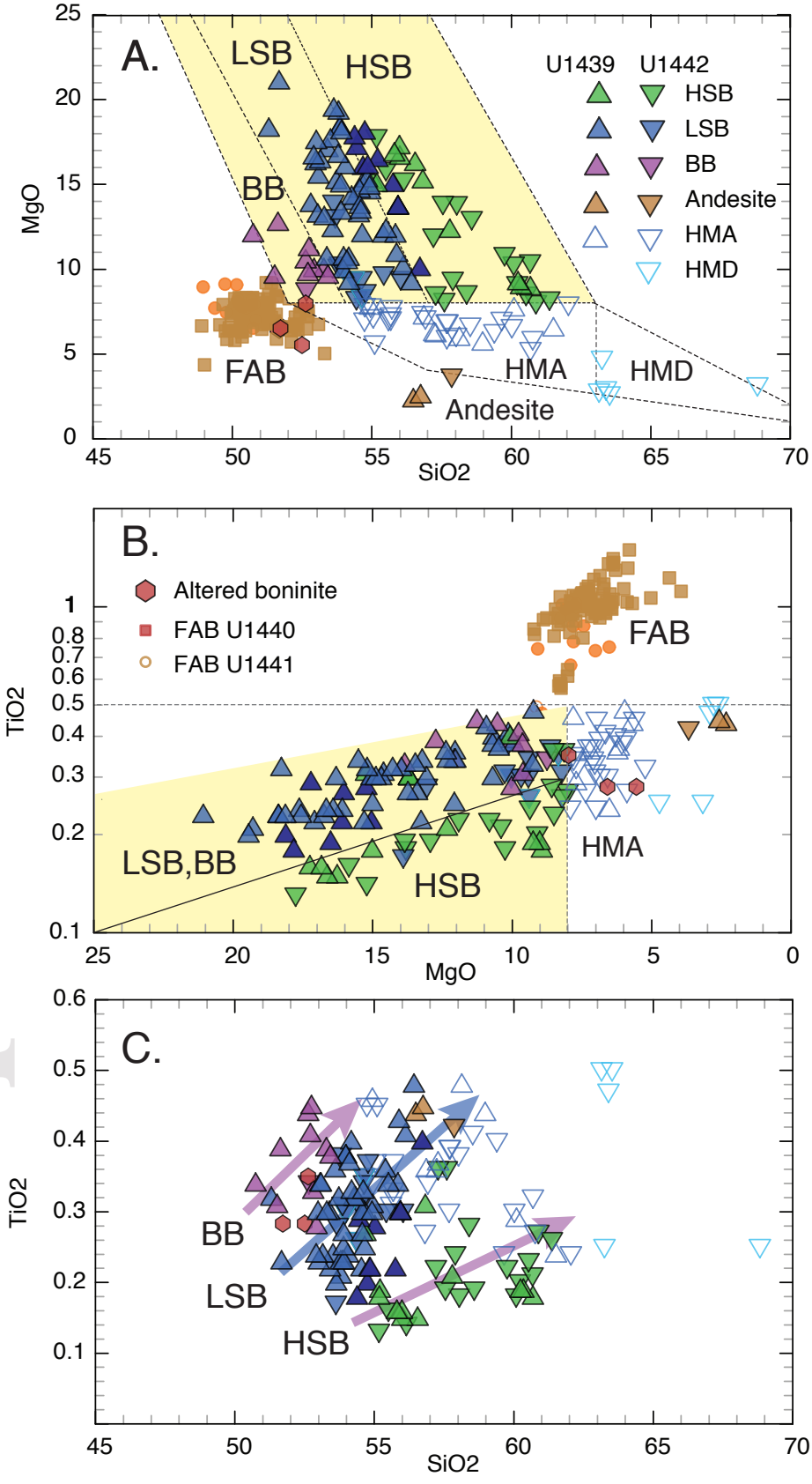

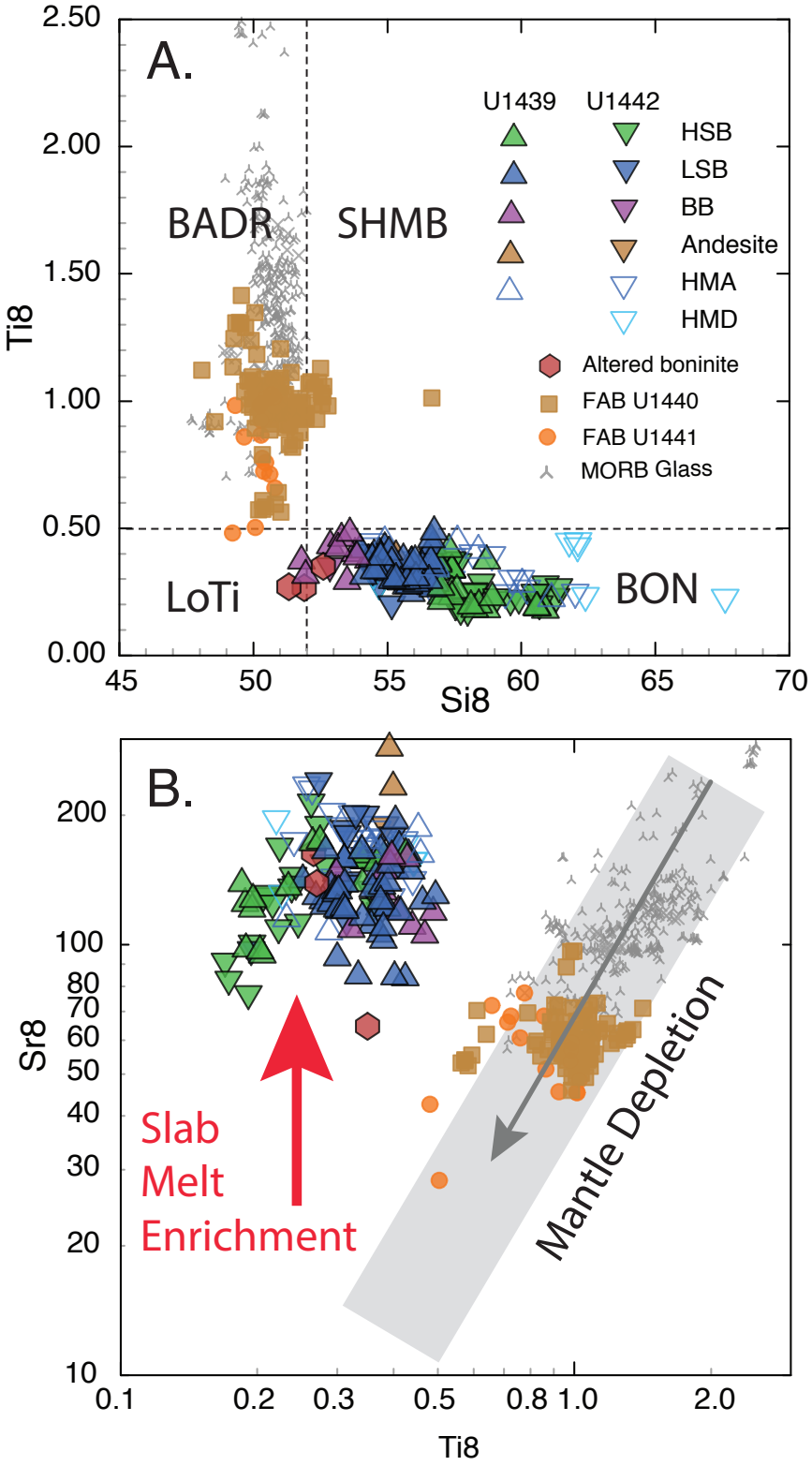


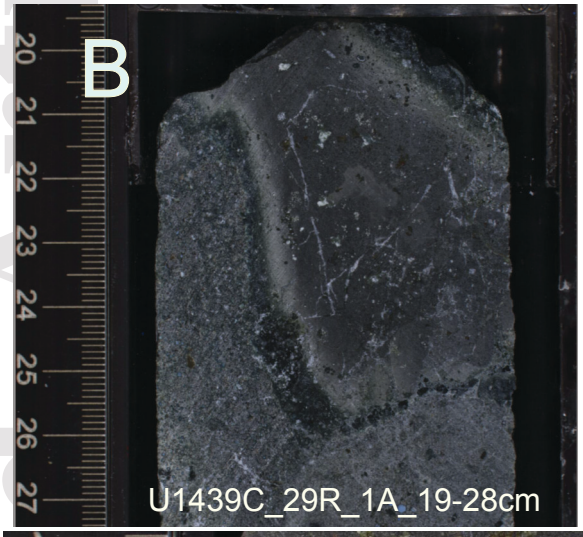


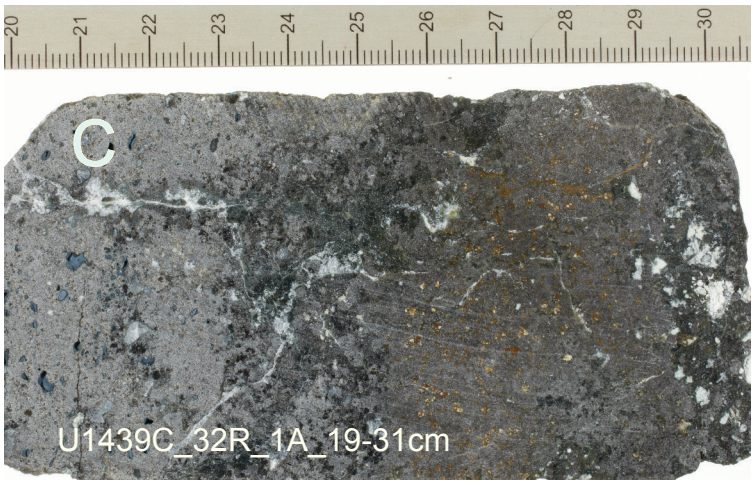


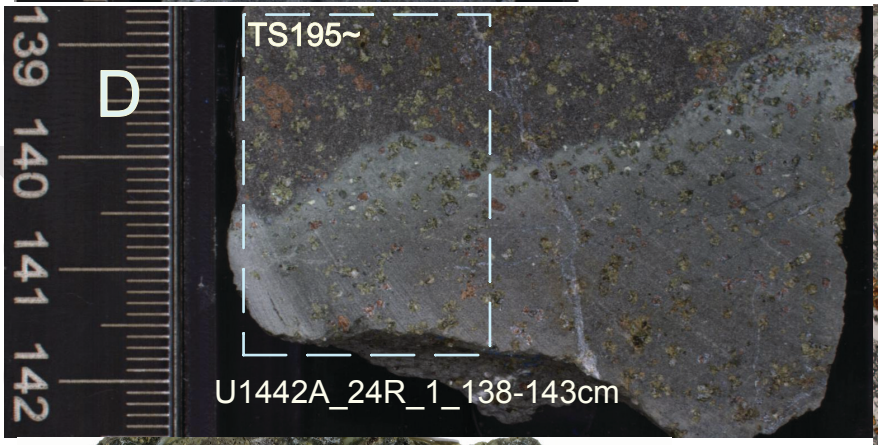


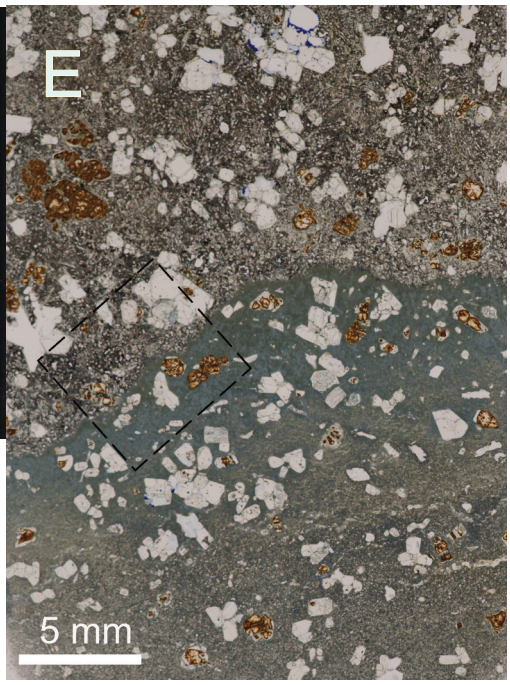


U1442A, 24R1 TS195

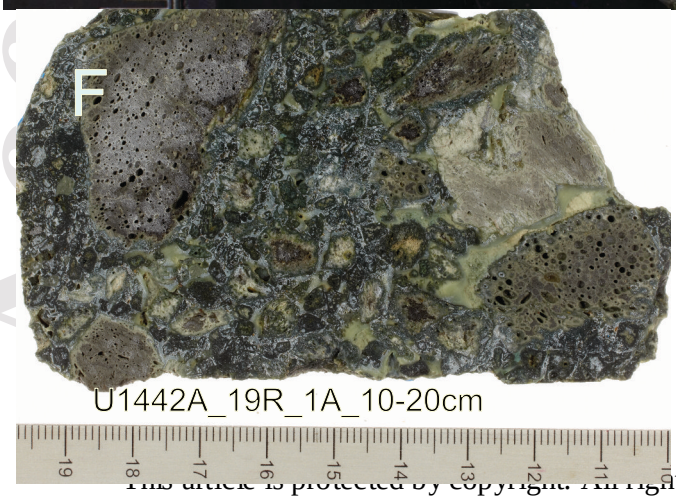

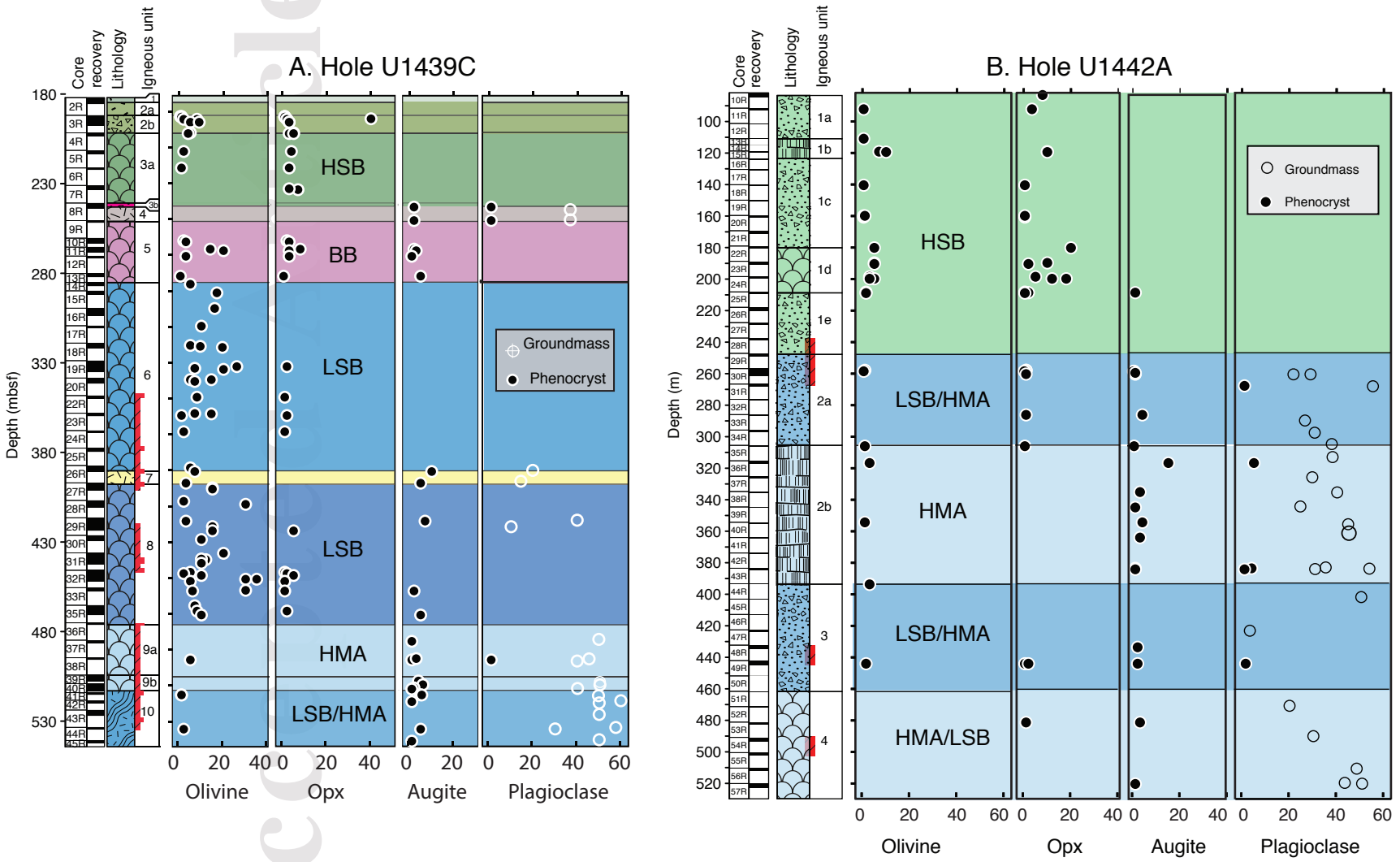

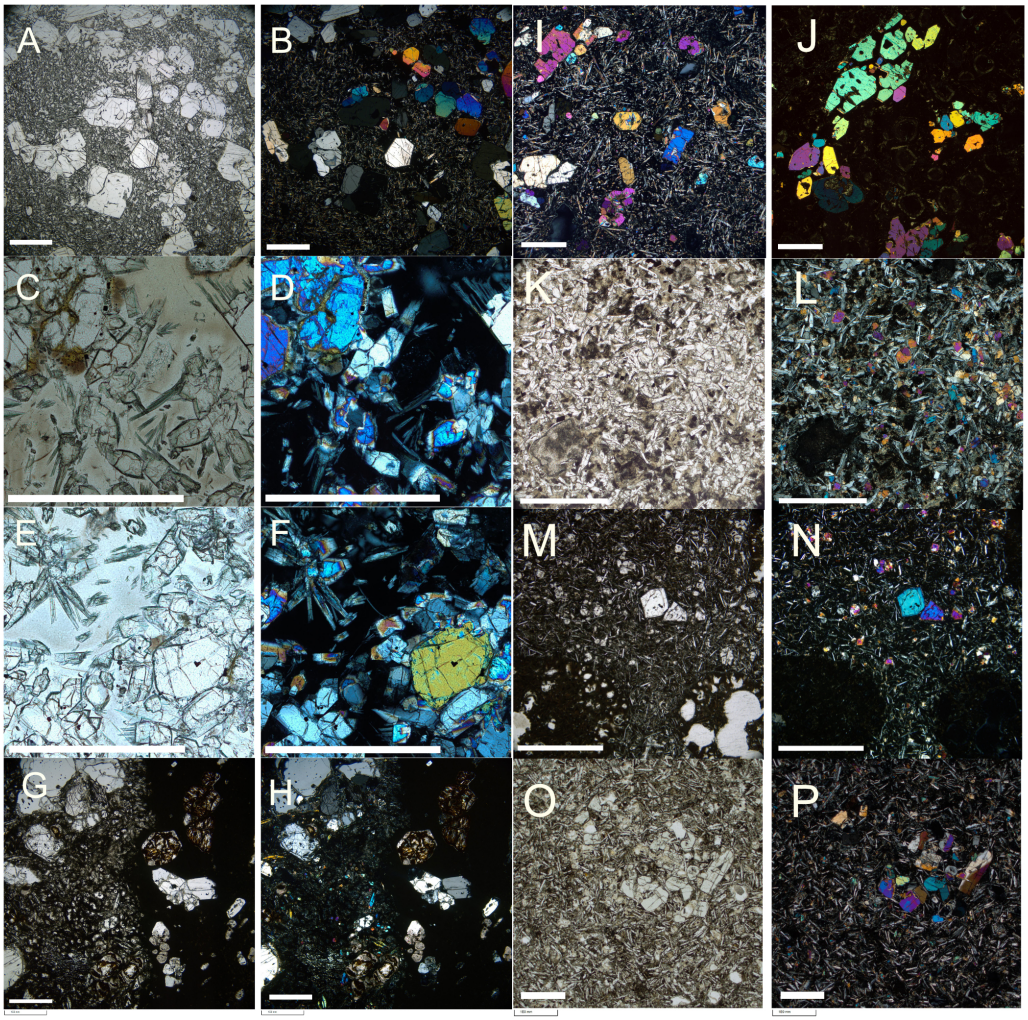

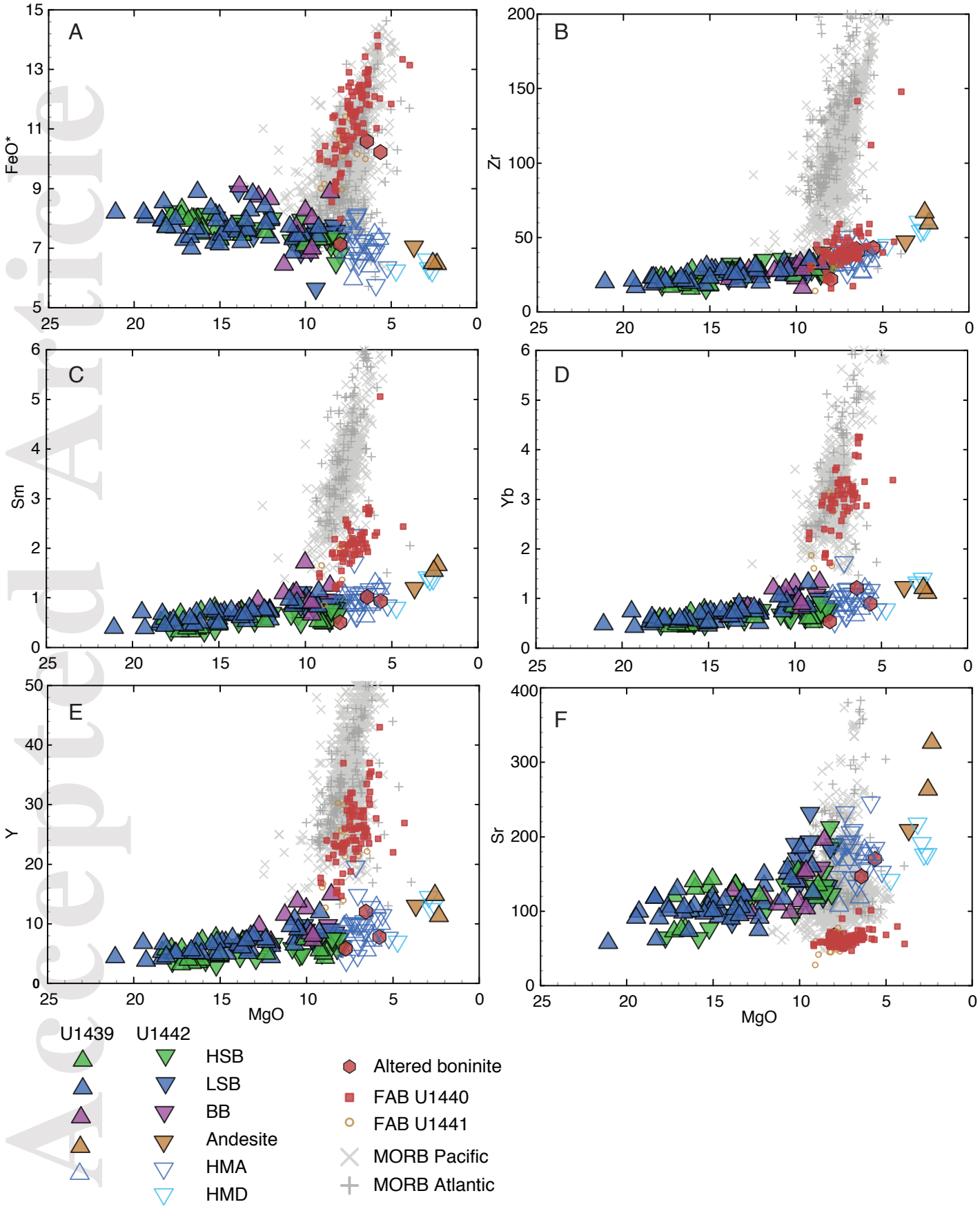

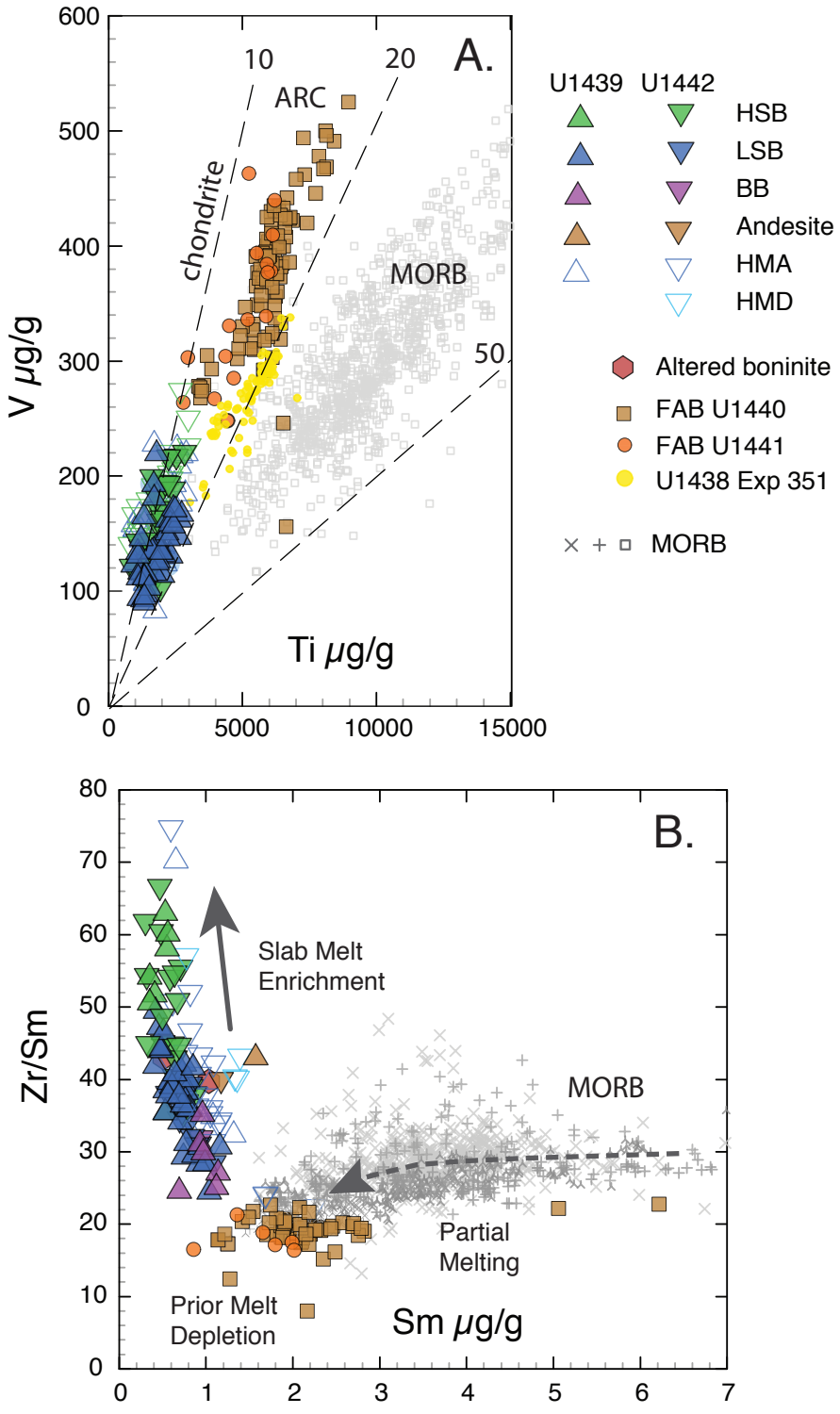

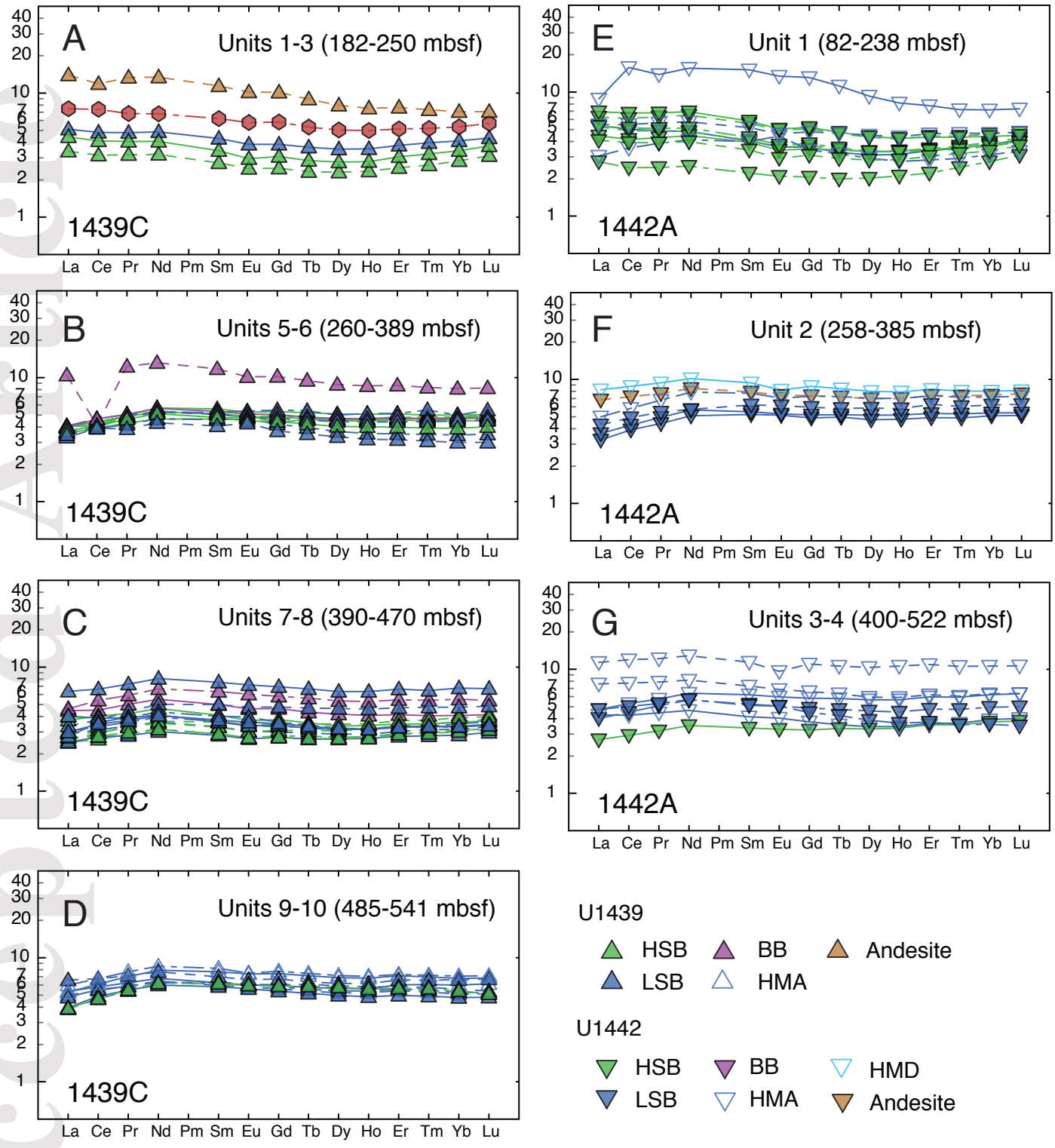

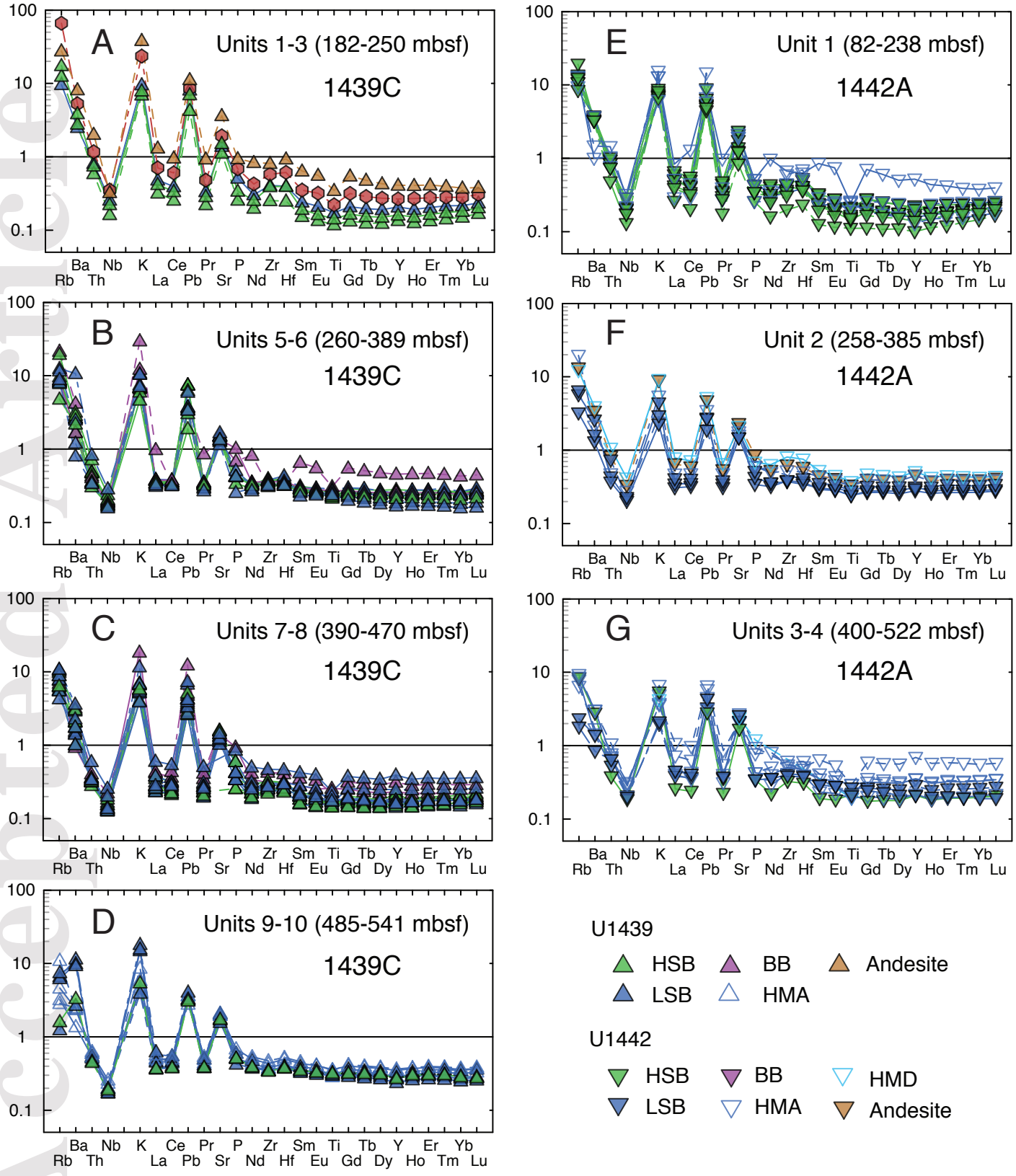

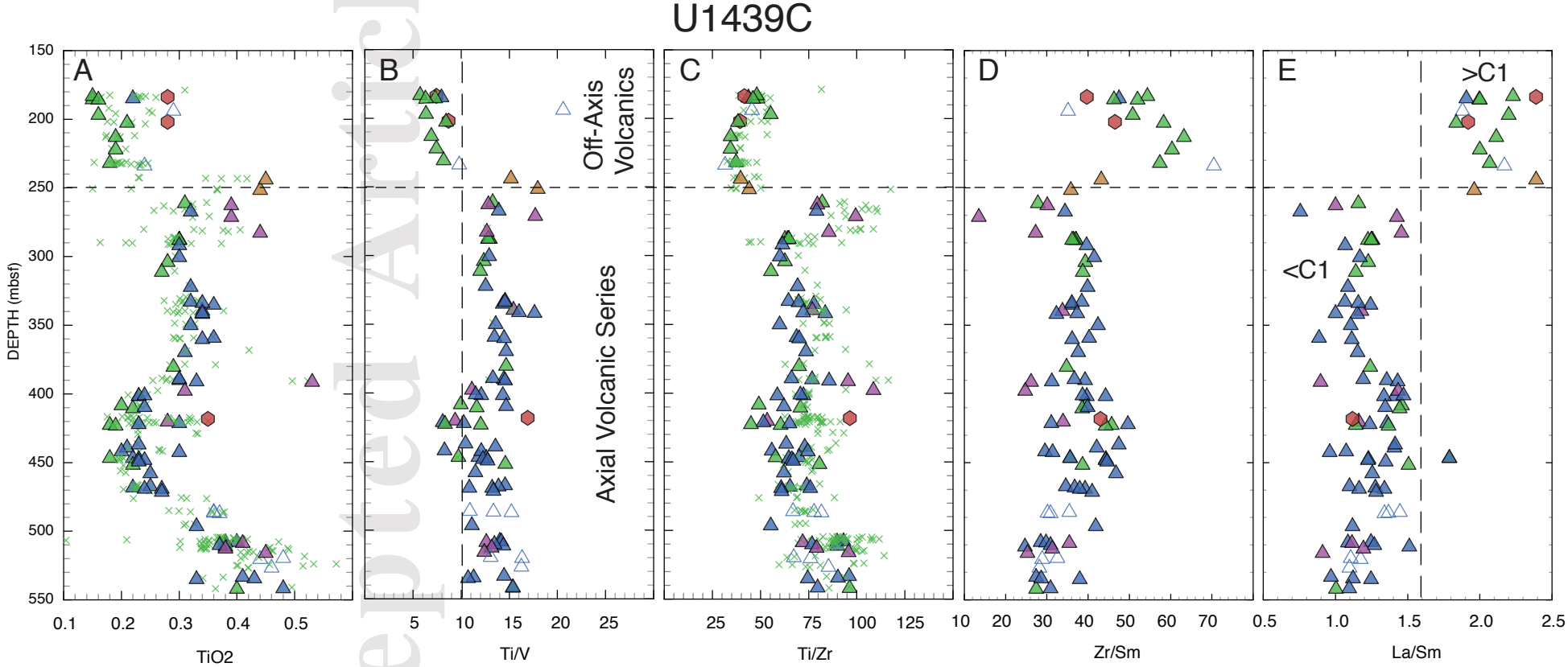

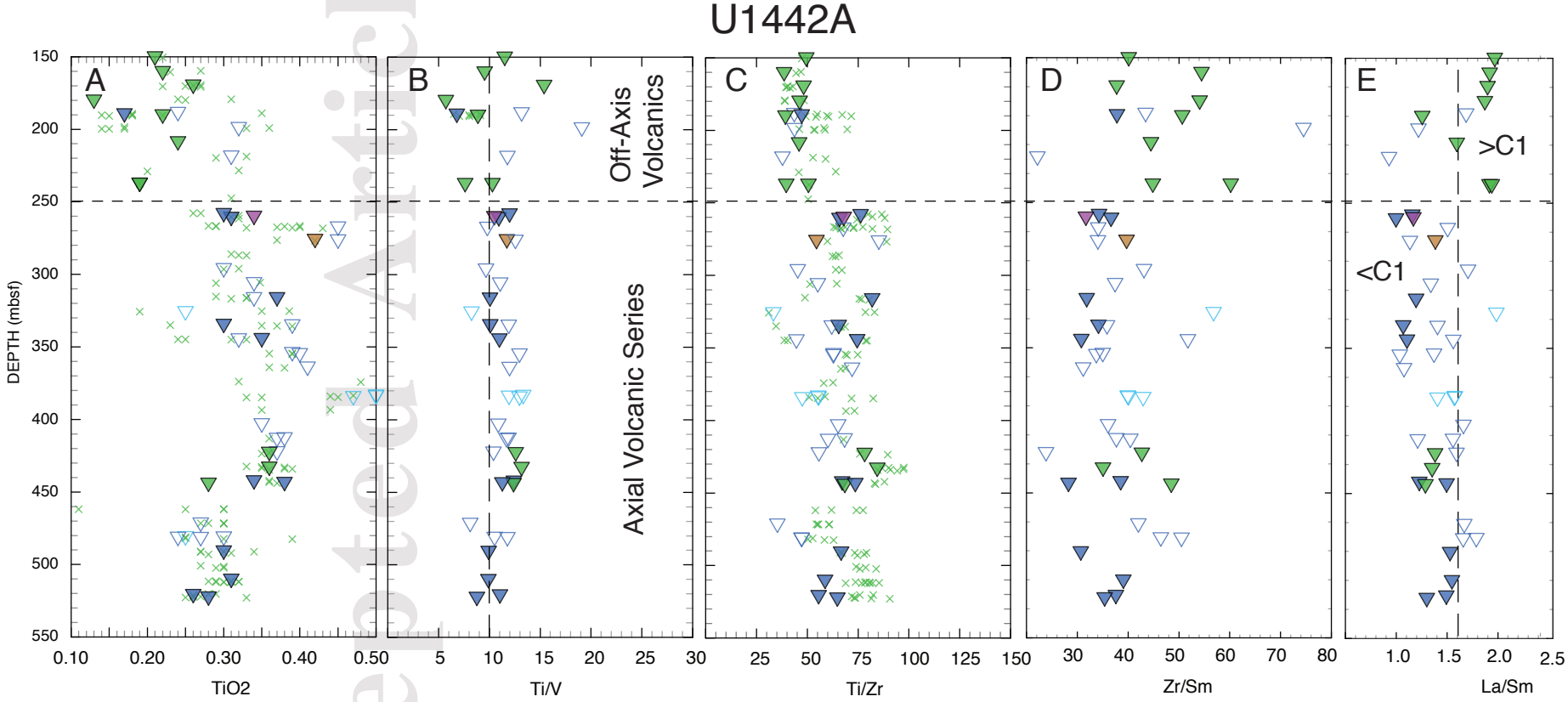

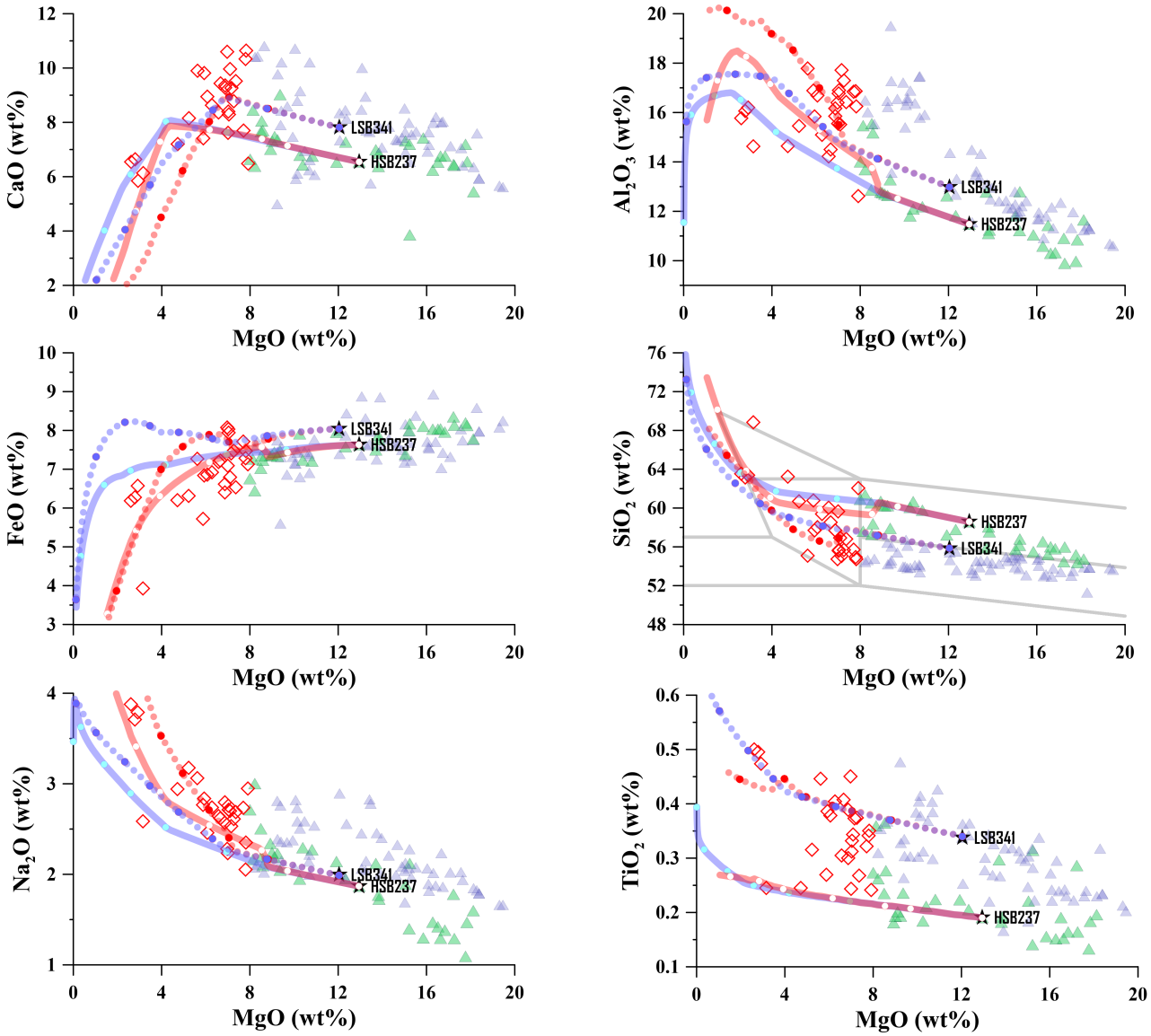


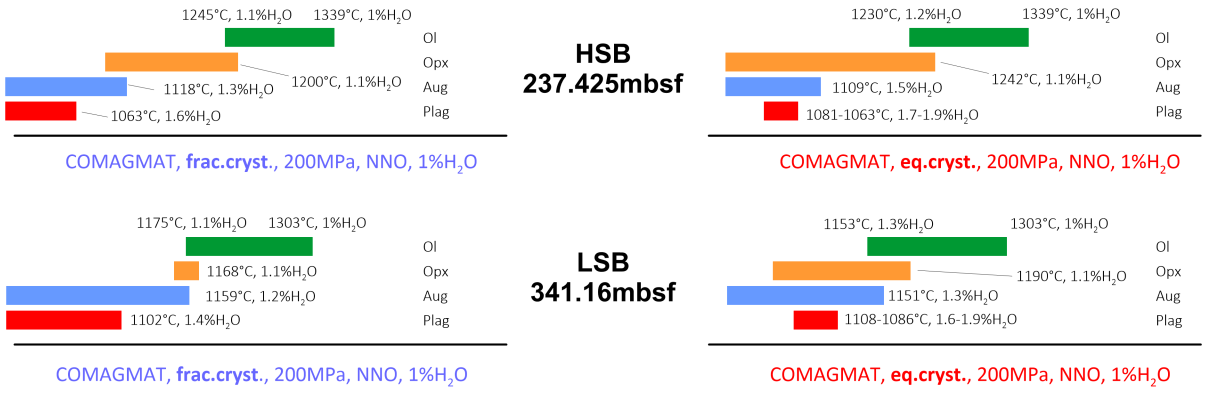


**Natural Samples**

- Bas. boninite whole rocks
- HSB whole rocks
- LSB whole rocks
- HMA

**Calculated LLD (with 10% step)**

- eq. cryst. HSB, 200MPa, 1%$H_2O$
- frac. cryst. HSB, 200MPa, 1%$H_2O$
- eq.cryst. LSB, 200MPa, 1%$H_2O$
- frac. cryst. LSB, 200MPa, 1%$H_2O$